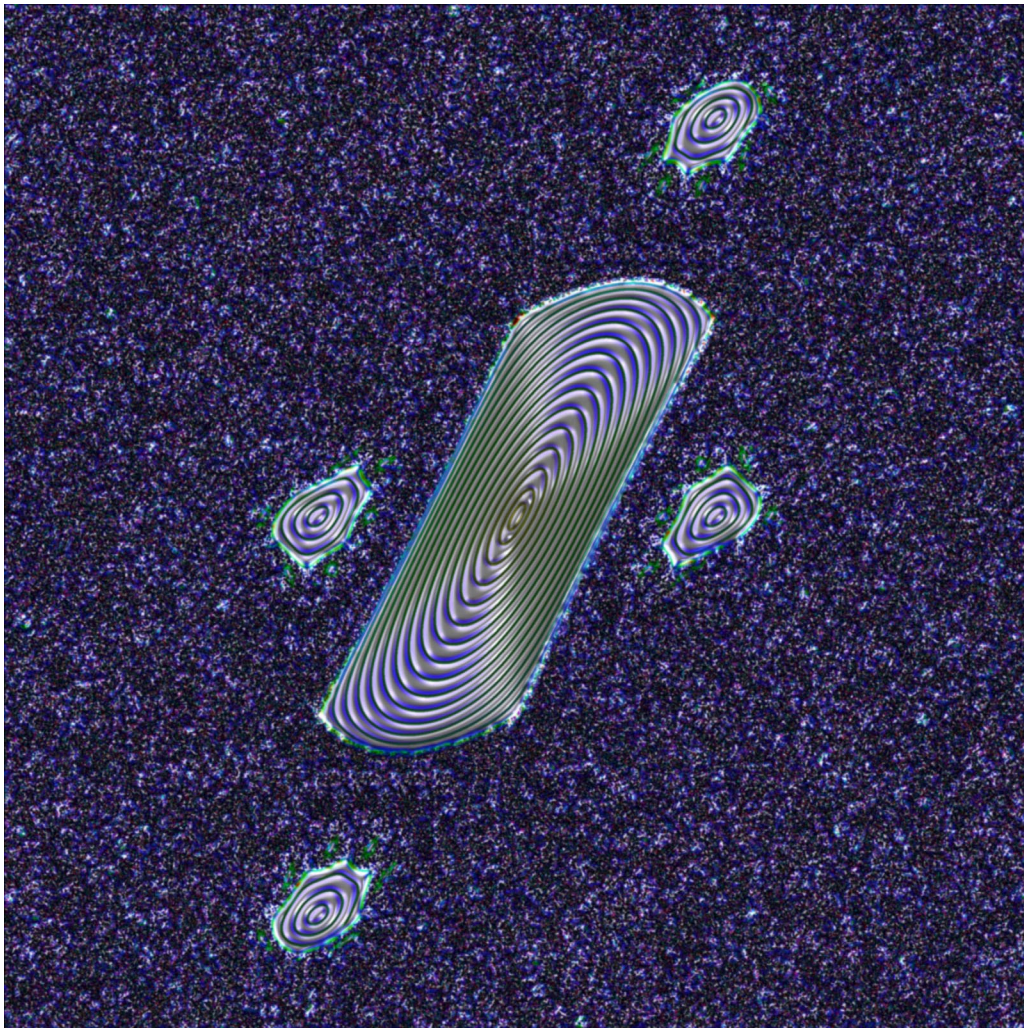


Chapter 4

Localization and Decoherence in the Kicked Rotor



4.1 Overview

Now we come to the first set of experiments discussed in this dissertation. In these studies, we focus on a realization of the kicked-rotor problem, formed by periodically pulsing on the optical standing wave. We will be concerned with the global (momentum) transport in the kicked rotor, since the classical and quantum transport are quite dramatically different due to dynamical localization. As we pointed out in Chapter 1, the difference between the quantum and classical behaviors is an apparent problem for correspondence. The goal of the research in this chapter is to directly address quantum–classical correspondence in the context of the kicked rotor. We will see that decoherence due to spontaneous emission or externally-imposed noise can destroy dynamical localization. Furthermore, we show that it is possible to obtain quantitative correspondence (at the global level of distributions and expectation values) in the presence of noise, even in a manifestly quantum regime.

The material presented in this chapter spans a number of previous publications from our group. The initial work on external noise and spontaneous emission effects was presented in [Klappauf98b]. The original confirmation of Shepelyansky’s quantum scaling and the observation of a nonexponential late-time distribution were both presented in [Klappauf98a]. The effects of the finite pulses in the experiment were characterized in [Klappauf99]. This earlier material is reviewed in [Klappauf98c], in more detail than we provide here. Later, we showed that we could observe ballistic transport at quantum resonance [Oskay00], even without sub-recoil velocity selection. The quantitative studies of noise effects on quantum localization and the return to the classical limit were presented in [Steck00; Milner00]. Finally, an experimental test of a universal quantum diffusion theory was presented in [Zhong01].

4.2 Rescaling

The atom-optics realization of the kicked rotor is described by the Hamiltonian

$$H(x, p, t) = \frac{p^2}{2m} + V_0 \cos(2k_L x) \sum_n F(t - nT) . \quad (4.1)$$

Here, T is the kick period, and $F(t)$ is a pulse function of unit height and duration $t_p \ll T$. Before proceeding, we will transform to scaled units to simplify our discussion, as we did for the pendulum in Chapter 1. As before, the spatial coordinate has a natural scaling,

$$x' := 2k_L x . \quad (4.2)$$

This time, however, there is a natural time scale for the problem, which defines the scaling of the time coordinate,

$$t' := t/T . \quad (4.3)$$

The corresponding scaling of the pulse is given by

$$f(t') := F(t)/\eta , \quad (4.4)$$

where we have defined the pulse integral

$$\eta := T^{-1} \int_{-\infty}^{\infty} F(t) dt \propto t_p, \quad (4.5)$$

so that the scaled pulse is normalized to unity (i.e., $\int_{-\infty}^{\infty} f(t) dt = 1$). If we define the constant

$$\tilde{k} := 8\omega_r T , \quad (4.6)$$

then the time scaling here is different from the pendulum time scaling by precisely this factor. This difference suggests that we should change the momentum scaling by the same factor,

$$p' := \frac{\tilde{k}}{2\hbar k_L} p . \quad (4.7)$$

Now the scaled coordinates obey the commutation relation,

$$[x', p'] = i\tilde{k} , \quad (4.8)$$

and thus we can interpret \tilde{k} as a scaled Planck constant, which can be “tuned” by varying the period T . More concretely, this parameter measures the action scale of the system in physical units compared to \hbar . We can then use the energy transformation $H' := (\tilde{k}/\hbar)TH$, and defining the stochasticity parameter as

$$K := \frac{\tilde{k}T}{\hbar} \eta V_0 , \quad (4.9)$$

the Hamiltonian in scaled units takes the form

$$H(x, p, t) = \frac{p^2}{2} + K \cos x \sum_n f(t - n), \quad (4.10)$$

after dropping the primes. In this way we have reduced the classical system to a single parameter (K) and the quantum system to two parameters (K and \hbar). Note that in these units, the constant \hbar also represents the quantization scale for momentum transfer, rather than unity as in the pendulum units or $2\hbar k_L$ in unscaled units.

4.3 Standard Map

In the limit of arbitrarily short pulses, the pulse function $f(t)$ is replaced by the Dirac delta function $\delta(t)$,

$$H(x, p, t) = \frac{p^2}{2} + K \cos x \sum_n \delta(t - n), \quad (4.11)$$

and this limit of the problem is commonly termed the “ δ -kicked rotor.” This limit is particularly convenient because the equations of motion can be reduced to a simple discrete map. From the form of the Hamiltonian (4.11), we note that during the kick, the potential term dominates the kinetic term. Between kicks, the potential term is zero, and the motion is that of a free rotor. Using these observations, we can integrate the equations of motion over one temporal period of the Hamiltonian.

Differentiating (4.11), Hamilton’s equations of motion become

$$\begin{aligned} \partial_t p &= -\frac{\partial H}{\partial x} = K \sin x \sum_{n=-\infty}^{\infty} \delta(t - n) \\ \partial_t x &= \frac{\partial H}{\partial p} = p. \end{aligned} \quad (4.12)$$

We will integrate Eqs. (4.12) to construct a map for x and p just *before* the n th kick. Letting ϵ be a small, positive number, we integrate the equation for p ,

$$\int_{t_n - \epsilon}^{t_{n+1} - \epsilon} \partial_t p(t) dt = \int_{t_n - \epsilon}^{t_{n+1} - \epsilon} K \sin x \sum_n \delta(t - n) dt, \quad (4.13)$$

where $t_n = n$ is the time of the n th kick. This equation then becomes

$$p(t_{n+1} - \epsilon) - p(t_n - \epsilon) = K \sin x. \quad (4.14)$$

Similarly, we integrate the equation for x ,

$$\int_{t_n - \epsilon}^{t_{n+1} - \epsilon} \partial_t x(t) dt = \int_{t_n - \epsilon}^{t_{n+1} - \epsilon} p dt , \quad (4.15)$$

which becomes

$$x(t_{n+1} - \epsilon) - x(t_n - \epsilon) = \epsilon p(t_n - \epsilon) + (1 - \epsilon) p(t_{n+1} - \epsilon) . \quad (4.16)$$

Then, letting $\epsilon \rightarrow 0$ and defining x_n and p_n to be the values of x and p just before the n th kick, we obtain the mapping

$$\begin{aligned} p_{n+1} &= p_n + K \sin x_n \\ x_{n+1} &= x_n + p_{n+1} . \end{aligned} \quad (4.17)$$

These equations, which constitute a one-parameter family of mappings parameterized by the *stochasticity parameter* K , are known as the *standard map* (or *Chirikov-Taylor map*), so named because of its broad importance in the study of Hamiltonian chaos. The significance of this widely studied map is due to both its simplicity, which makes it amenable to both analytical and numerical study, and the fact that many systems can be locally approximated by the standard map [Chirikov79].

A number of standard-map phase plots are shown in Appendix B. The phase space for the standard map is clearly invariant under a 2π translation in x , because of the corresponding invariance of the mapping itself, and so x is usually taken to be within the interval $[0, 2\pi)$. What is perhaps less obvious is that the phase-space structure is also invariant under a 2π translation in p , as well. This point is more easily recognized from the Hamiltonian of the δ -kicked rotor (for which the standard-map phase space is a Poincaré section). Using a form of the Poisson sum rule,

$$\sum_{n=-\infty}^{\infty} \delta(t - n) = \sum_{n=-\infty}^{\infty} \cos(2\pi n t) , \quad (4.18)$$

we can rewrite the δ -kicked rotor Hamiltonian as

$$\begin{aligned} H(x, p, t) &= \frac{p^2}{2} + K \cos x \sum_{n=-\infty}^{\infty} \cos(2\pi n t) \\ &= \frac{p^2}{2} + \sum_{n=-\infty}^{\infty} K \cos(x - 2\pi n t) . \end{aligned} \quad (4.19)$$

From this form of the Hamiltonian, it is apparent that the δ -pulsed potential can be regarded as a superposition of an infinite number of unmodulated pendulum potentials moving with momentum $2\pi n$ for every integer n . The Hamiltonian is therefore invariant under boosts of $2\pi n$ in momentum, so the phase space is 2π -periodic in both x and p . Each of these pendulum terms is associated with a primary nonlinear resonance in the phase space, located at $(x, p) = (\pi, 2\pi n)$, and the interactions between these resonances result in chaos and rich structure in phase space.

4.4 Classical Transport

We will now consider the global behavior in the standard map. In particular, we will consider the transport in the limit of large K , where the phase space is predominantly chaotic (which operationally means $K \gtrsim 5$). Also in this limit, there are no Kolmogorov-Arnol'd-Moser (KAM) surfaces that span the phase space, dividing the phase space in the momentum direction and preventing chaotic transport to arbitrarily large momenta (this is true for any K above the Greene number, $K_G \approx 0.971635$ [Greene79]). Broadly speaking, invariant surfaces (KAM surfaces, which are traceable to invariant surfaces in the integrable limit, and islands of stability) confine trajectories, while chaotic trajectories are free to ergodically wander throughout the chaotic region. In the next section we will find that the chaotic motion can be thought of as being diffusive (like a random walk), although the presence of small but nevertheless important islands of stability complicate this diffusion picture.

4.4.1 Diffusion and Correlations

Focusing on the momentum transport in the standard map, we use the first equation in the standard map (4.17) to calculate the kinetic energy of a trajectory ensemble after n iterations:

$$\begin{aligned} E_n &:= \frac{\langle p_n^2 \rangle}{2} \\ &= \frac{1}{2} \sum_{m, m'=0}^{n-1} C_{m-m'} . \end{aligned} \quad (4.20)$$

Here, the correlation functions C_m are defined as

$$C_{m-m'} := \langle K \sin x_m K \sin x_{m'} \rangle . \quad (4.21)$$

(A similar discussion along these lines can be found in [Cohen91], but with a slightly different definition for the correlations.) The angle brackets here denote an average over the initial ensemble. For the purposes of the present analysis, we can take this average to be uniform over the unit cell in phase space, which is appropriate for the initial distribution of MOT atoms for the experimental parameters (for which the distribution is broad in both x and p compared to the unit cell size). The correlations also obviously depend only on the difference $m - m'$, as there is no explicit time dependence in the standard map.

The sum in Eq. (4.20) can be straightforwardly evaluated if one makes the approximation that the coordinate x_n is uniform and uncorrelated, as one might expect for very large K when the phase space is almost entirely chaotic. Doing so allows one to ignore the off-diagonal terms in the sum and gives the result

$$E_n = \frac{C_0}{2}n = \frac{K^2}{4}n . \quad (4.22)$$

The energy growth is hence diffusive (linear in time), with diffusion rate $D_{\text{ql}}(K) = K^2/4$, which is known as the *quasilinear* diffusion rate. This quasilinear (random-phase) approximation is equivalent to assuming that the motion is a random walk in momentum, and thus the momentum distribution is asymptotically Gaussian with a width $\sim \sqrt{n}$.

The random-phase approximation is only valid in the limit of arbitrarily large K , however, and for finite K the higher-order correlations cannot always be neglected, even for trajectories within the chaotic region of phase space. Nonuniformities in the chaotic region, especially near the borders of stability islands, can lead to nonzero correlations, and thus to deviations of the diffusion rate from the quasilinear value. A more general expression for the (time-dependent) diffusion rate in terms of the higher-order correlations is

$$D_n := E_{n+1} - E_n = \frac{1}{2} \sum_{m=-n}^n C_m . \quad (4.23)$$

These corrections to the diffusion rate were treated analytically in [Rechester80; Rechester81], where the series (4.23) was shown to be an asymptotic expansion in powers of Bessel functions of K . The result from [Rechester81] is

$$D(K) = \frac{K^2}{2} \left(\frac{1}{2} - J_2(K) - J_1^2(K) + J_2^2(K) + J_3^2(K) \right) \quad (4.24)$$

to second order in the Bessel functions (we defer the derivation of these results to Section 4.8). This expression represents the rate D_n of energy diffusion for long times n and large values of K ; the higher-order terms in the expansion are assumed at this point to have only a small contribution, since they represent higher powers of $1/\sqrt{K}$. In this expression, it is often convenient to neglect $J_3^2(K) - J_1^2(K)$, which is $O(K^{-2})$, since for large K this difference is much smaller than $J_2^2(K)$, which is $O(K^{-1})$; however, these terms will be important when generalizing this result to account for amplitude noise below. This result shows that $D(K)$ oscillates about the quasilinear value, where the corrections become small compared to the quasilinear value as K becomes large.

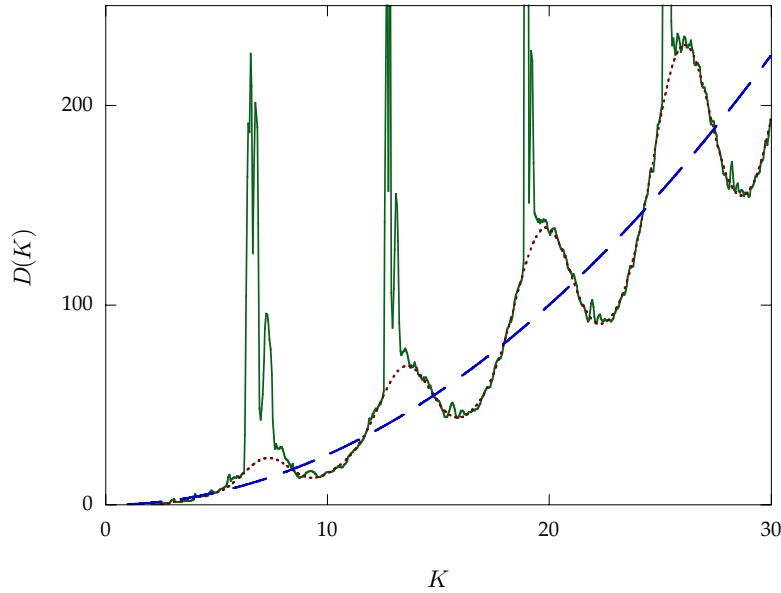


Figure 4.1: Dependence of the rate of energy diffusion D on the stochasticity parameter. The analytical diffusion expression [Eq. (4.24), dotted line] shows a significant oscillatory departure from the quasilinear prediction (dashed line). The simulated diffusion rate (solid line) is computed assuming an initial condition of 10^5 particles distributed uniformly over a unit cell in phase space, and is averaged over 1000 iterations of the standard map. The simulation agrees with Eq. (4.24) except at the peaks of the diffusion curve, where the diffusion is dramatically enhanced by the influence of accelerator modes.

4.4.2 Accelerator Modes

The diffusion rate expression in Eq. (4.24) is plotted in Fig. 4.1 along with the diffusion rate calculated in a simulation. The agreement is generally good, with the exception of the peaks in the diffusion curve, where the simulated diffusion rate greatly exceeds the analytical prediction. This discrepancy stems from the fact that we have so far assumed that the chaos causes the correlation series (4.23) to drop off rapidly (i.e., exponentially). However, the presence of small, stable islands (which are present for any value of K) can make the longer time correlations important, so that the correlation series decays slowly (i.e., like a power law [Karney83; Chirikov84]), and as a result this series may not even rigorously converge.

The stable structures that cause the large deviations in Fig. 4.1 are the *accelerator modes* [Chirikov79; Ishizaki91; Klafter96]. These structures are different from the usual stability islands in that they are boosted by a constant amount in momentum on each iteration. The main family of accelerator modes occur in the stability windows $(2\pi j) < K < \sqrt{(2\pi j)^2 + 16}$ (for integer j), where the corresponding accelerator mode hops monotonically by $2\pi j$ in momentum per iteration [Chirikov79]. These intervals are precisely the locations of the strong deviations in Fig. 4.1; note that the $j = 0$ case simply corresponds to the primary resonances, as we discussed in the context of Eq. (4.19), whereas for $j > 0$ the accelerator modes are born by tangent bifurcations. From the inversion-symmetry properties of the standard map (i.e., invariance under the combined transformation $p \rightarrow -p, x \rightarrow -x$), we can see that the accelerator modes occur in pairs, which “stream” in opposite senses. The accelerator modes are obviously a peculiarity of the standard map, a result of the periodicity of the phase space in the momentum direction. Other systems, such as the experimental realization of the kicked rotor (which uses finite, not δ -function, kicks) can still exhibit *quasiaccelerator modes*, which behave like accelerator modes over a bounded region in phase space [Lichtenberg92].

The behavior of the trajectories trapped within stable islands and accelerator modes is clearly different in nature from that of chaotic trajectories. However, these coherent phase-space structures can still have a strong influence over the behavior of chaotic trajectories. The boundaries of the islands, where the stable regions merge into the surrounding chaotic sea, are

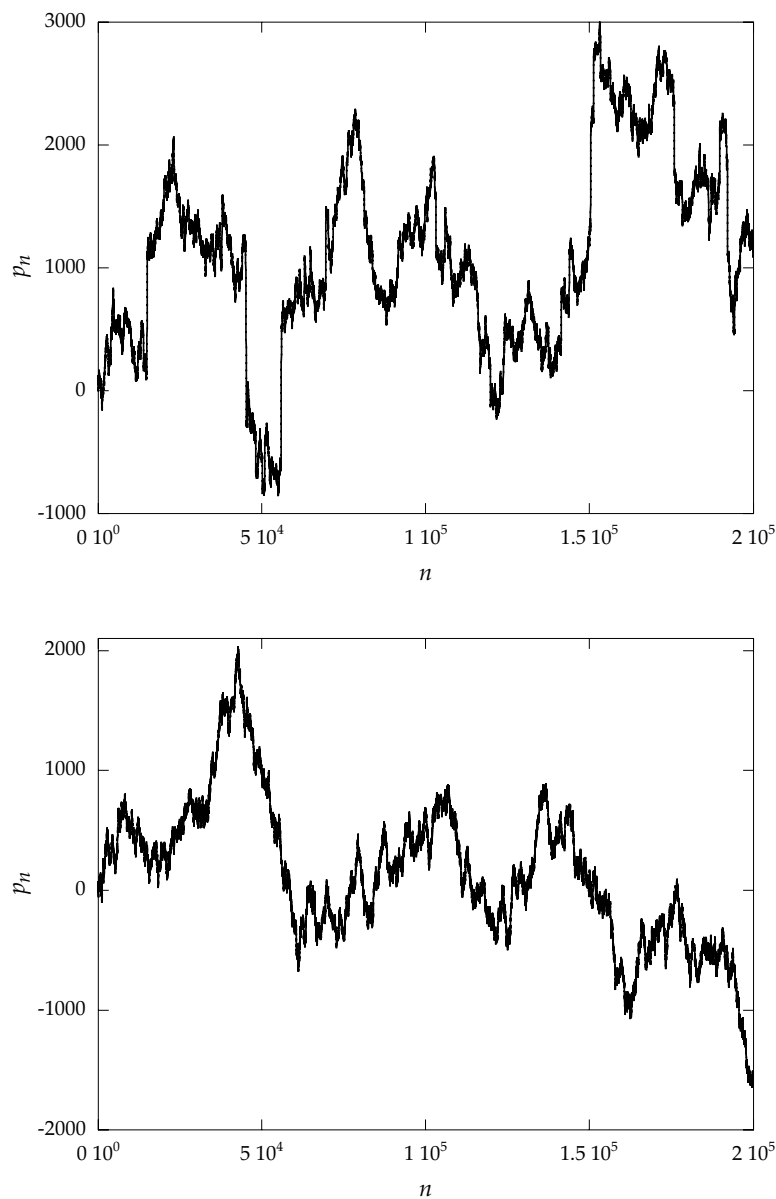


Figure 4.2: Upper graph: plot of the iterates p_n for a standard-map trajectory in the presence of accelerator modes, showing Lévy-flight behavior. The stochasticity parameter is $K = 6.52$, and the initial condition is $(x_0, p_0) = (3, 3.5)$. The Lévy flights are apparent as sudden jumps in momentum as a result of many successive steps in the same momentum direction. Lower graph: plot of the iterates p_n for a standard-map trajectory showing normal diffusive behavior. The stochasticity parameter is $K = 9.5$, and the initial condition is $(x_0, p_0) = (3, 3.5)$.

complicated and fractal in nature. This structure causes the island boundaries to be “sticky” in the sense that chaotic trajectories can become trapped for some finite time in the boundary layer. As the chaotic trajectories wander throughout the phase space, they will eventually wander close enough to any island to become trapped. The self-similar structure of the boundary causes these trapping times to have a power-law distribution [Karney83], and the resulting dynamics are characterized by Lévy-flight behavior, rather than simple diffusion [Klafter96]. The regular stability islands tend to trap trajectories at a fixed momentum, leading to reduced momentum transport, whereas the accelerator modes lead to streaming (with many correlated momentum steps), and therefore to enhanced momentum transport. This subdiffusive or superdiffusive behavior due to island structures is referred to as *anomalous diffusion* [Chirikov84; Geisel87; Klafter96; Benkadda97; Zumofen99]. The momentum distribution in this regime has asymptotically power-law tails, rather than Gaussian tails, and the kinetic energy scales as $E(t) \sim t^\mu$, where the transport exponent $\mu \neq 1$ for anomalous diffusion. The Lévy flights in a standard-map trajectory are apparent in Fig. 4.2, especially compared to a diffusive trajectory, shown also in this figure.

As the transport in the standard map is not strictly diffusive, the proper framework for the global dynamics is fractional kinetics [Zaslavsky97; Saichev97; Zaslavsky99]. However, since the stable islands in phase space are typically small for large K (the areas of the islands are asymptotically of the order K^{-2} [Chirikov79]), it may take many kicks before the islands cause large deviations from diffusive behavior. Hence, for the time scales observed in our experiments (up to 80 kicks), it is appropriate to describe the classical dynamics as diffusive as long as large accelerator modes are not present. Operationally, Eq. (4.24) is an excellent approximation away from the main family of accelerator modes.

4.4.3 External Noise

The transport that we have studied is heavily influenced by correlations, and we might expect that noise will therefore also have substantial effects on the global dynamics. One type of decohering interaction that we will study more in Section 4.5.4 is spontaneous emission. To model

the effects of spontaneous emission in the standard map, we could simply consider a fluctuating momentum perturbation that models the random momentum recoil of the atom in response to the photon scattering. We can compare this situation qualitatively to the results of Ref. [Karney82] (see also [Lichtenberg92]), which considers the generalized (noisy) mapping

$$\begin{aligned} p_{n+1} &= p_n + K \sin x_n + \delta p_n \\ q_{n+1} &= q_n + p_{n+1} + \delta x_n \ , \end{aligned} \quad (4.25)$$

where δp_n and δx_n are time-dependent random variables. In the case where δp_n and δx_n are chosen from a normal distribution, the diffusion rate from Eq. (4.24) becomes

$$\begin{aligned} D(K) &= \frac{K^2 + 2\rho^2}{4} + \frac{K^2}{2} \left[-J_2(K)e^{-(\sigma^2 + \rho^2/2)} \right. \\ &\quad \left. - J_1^2(K)e^{-(\sigma^2 + \rho^2)} + J_2^2(K)e^{-(2\sigma^2 + \rho^2)} + J_3^2(K)e^{-(3\sigma^2 + \rho^2)} \right] , \end{aligned} \quad (4.26)$$

where ρ^2 is the variance of δp_n , and σ^2 is the variance of δx_n . The noise therefore affects the diffusion by exponentially damping the higher-order correlations, and the momentum perturbation also gives a direct contribution to the quasilinear term.

For the quantitative comparison of quantum and classical dynamics of the kicked rotor in Section 4.6, we used amplitude noise, where the value of K is randomly varied from kick to kick. This interaction has the advantage of being easy to apply and quantify compared to other decohering interactions such as spontaneous emission. We can also treat the effects of this noise on the classical correlations analytically, as we now discuss (again, some of the more gruesome details are left to Section 4.8). The standard map including amplitude noise is

$$\begin{aligned} p_{n+1} &= p_n + (K + \delta K_n) \sin x_n \\ q_{n+1} &= q_n + p_{n+1} \ , \end{aligned} \quad (4.27)$$

where δK_n is a random deviation for the n th kick, distributed according to $P(\delta K)$, with zero mean. The noise again modifies the correlations, and the generalization of (4.21) is

$$\begin{aligned} C_{m-m'} &= \int d(\delta K_m) \cdots d(\delta K_{m'}) P(\delta K_m) \cdots P(\delta K_{m'}) \\ &\quad \times \langle (K + \delta K_m) \sin x_m (K + \delta K_{m'}) \sin x_{m'} \rangle , \end{aligned} \quad (4.28)$$

where there are $|m - m'| + 1$ integrals over the kick probability distribution, because the coordinate at the later time depends on all the kicks after the earlier time. As we can see from

Section 4.8, each factor of K (the two factors of K and several factors of $J_n(K)$) in Eq. (4.24) enters as an independent random variable, so that the integration in (4.28) amounts to averaging over each factor independently. The resulting generalization of (4.24) is

$$D(K) = \frac{K^2 + \text{Var}(\delta K)}{4} + \frac{K^2}{2} (-\mathcal{J}_2(K) - \mathcal{J}_1^2(K) + \mathcal{J}_2^2(K) + \mathcal{J}_3^2(K)). \quad (4.29)$$

In this equation, $\text{Var}(\delta K)$ denotes the variance of $P(\delta K)$, and

$$\mathcal{J}_n(K) := \int_{-\infty}^{\infty} P(\delta K) J_n(K + \delta K) d(\delta K). \quad (4.30)$$

This expression makes it immediately clear how amplitude noise affects the diffusion rate: the integral in Eq. (4.30) is analogous to a convolution of the Bessel functions with the noise distribution. As the noise level is increased, the Bessel functions are smoothed out, and the correlations are effectively destroyed. This is especially true for long-term correlations, and indeed anomalous diffusion is suppressed in the presence of noise. At the same time, there is an increase in the quasilinear diffusion component, because the fluctuating kick strength leads to a fluctuating momentum perturbation, but this effect is generally small in comparison to the destruction of the correlations.

In the experiments, we considered exclusively the case of amplitude noise with a uniform probability distribution,

$$P(\delta K) = \begin{cases} 1/\delta K_{p-p}, & \delta K \in (-\delta K_{p-p}/2, \delta K_{p-p}/2) \\ 0 & \text{elsewhere,} \end{cases} \quad (4.31)$$

where δK_{p-p} is the peak-to-peak deviation of the kick strength. When we quote the noise level used in our experiments, we are quoting the normalized peak-to-peak deviation $\delta K_{p-p}/K$. For this noise, the variance, which characterized the contribution to the quasilinear diffusion, is $\text{Var}(\delta K) = (\delta K_{p-p})^2/12$, and from Eq. (4.30), the correlation contributions to the diffusion in (4.24) are simply convolved with a “box” window. For illustration, the function (4.29) is plotted for several different levels of amplitude noise in Fig. 4.3. Notice that for the 100% and 200% noise levels, the correlations are essentially destroyed, so that these noise levels cannot be considered perturbative; however, these noise levels are still small in the sense that their contribution to the quasilinear diffusion rate is significantly smaller than the zero-noise component.

4.4.4 Finite-Pulse Effects

In a real experiment, we obviously cannot realize exact δ -kicks, but we can use short laser pulses to work near this limit. The standard map is a valid model of the finite-pulse kicked rotor if the motion of the atom is negligible throughout the duration of the pulse, because this situation mimics the strobe-like nature of the δ -function pulses. This observation implies that the δ -kick approximation is valid within a bounded interval in momentum about $p = 0$. We can obtain a crude estimate for the momentum at which the δ -kick approximation breaks down by considering an atom moving with a velocity such that it travels over one period of the optical lattice over the duration t_p of the pulse. The momentum transferred to the atom is approximately zero, and thus the momentum p_b for this “boundary” is

$$\frac{p_b}{2\hbar k_L} = \frac{m\lambda^2}{8\pi\hbar t_p}, \quad (4.32)$$

where all quantities are in physical units. The dependence of this boundary on the atomic mass m and the lattice wavelength λ motivated the use of a cesium-based apparatus for these

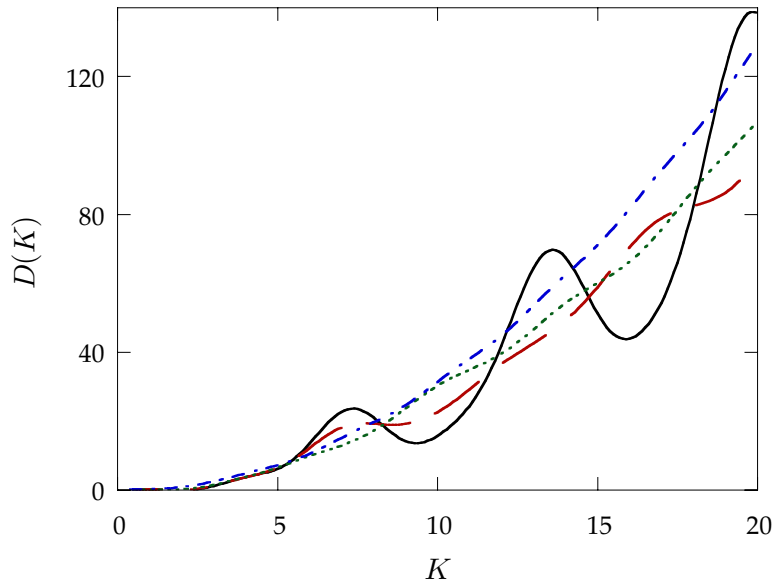


Figure 4.3: Plot of the diffusion expression (4.29) for several levels of amplitude noise (with uniformly-distributed statistics): no noise (solid line), 50% noise (dashed line), 100% noise (dotted line), and 200% noise (dot-dashed line). The oscillations, which represent short-term correlations, are smoothed out by the noise.

experiments over the previous sodium-based apparatus, in order to realize an increase in $p_b/2\hbar k_L$ by a factor of 12 for fixed t_p .

We can make this momentum boundary effect due to finite pulses more precise by reconsidering the form (4.19) for the kicked-rotor Hamiltonian. We can write the kicked-rotor Hamiltonian (4.10) for finite pulses as

$$H(x, p, t) = \frac{p^2}{2} + K \cos x \sum_{j=-\infty}^{\infty} c_j e^{-i2\pi j t}, \quad (4.33)$$

where the Fourier coefficient c_j is given by

$$c_j = \int_0^1 \sum_n f(t-n) e^{i2\pi j t} dt. \quad (4.34)$$

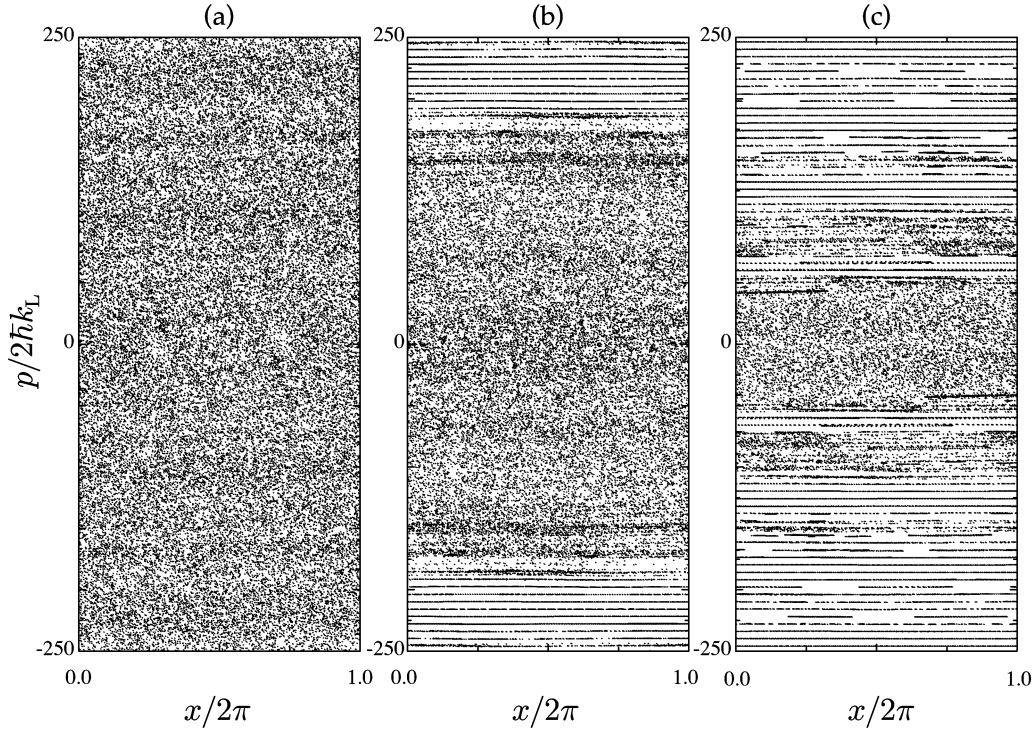


Figure 4.4: Phase-space plots for the kicked rotor with $K = 10.5$ in the cases of (a) δ -kicks, (b) square pulses with pulse width $t_p/T = 0.014$, and (c) square pulses with $t_p/T = 0.049$. Case (b) is similar to the pulses used in the experiments in this chapter. The effect of the finite pulses is to introduce KAM surfaces at large momenta in the otherwise chaotic phase space.

This Hamiltonian can in turn be rewritten as

$$H(x, p, t) = \frac{p^2}{2} + K \sum_{j=-\infty}^{\infty} |c_j| \cos(x - 2\pi jt + \phi_j) \quad , \quad (4.35)$$

where we have defined the phases of the coefficients by $c_j = |c_j| \exp(i\phi_j)$, and we have used the fact that $c_j = c_{-j}^*$. Also, from the definition of $f(t)$, the coefficient c_0 of the stationary term is unity. In the case of δ -kicks, we saw that $c_j = 1$ holds true for all the coefficients. However, for finite pulses the Fourier weights drop off with increasing j , so that the primary resonances are attenuated at large momentum. Larger pulse widths imply a narrower spectrum, and hence a boundary at lower momentum, as we discovered using the simpler estimate above.

The effects of finite pulses are illustrated in Fig. 4.4, which shows the phase space for a δ -kicked rotor compared with two phase spaces corresponding to kicks with square pulse profiles. For the case of square pulses, we can define a momentum-dependent effective stochasticity parameter based on the Fourier transform argument as

$$K_{\text{eff}}(p) = K \text{sinc} \left(\frac{t_p p}{2} \right) \quad , \quad (4.36)$$

where $\text{sinc}(x) = \sin(x)/x$, and p and t_p are scaled variables. This sinc profile is especially apparent in Fig. 4.4(c), where the phase space becomes stable as K_{eff} drops below ~ 1 (recall that the “stochasticity border” for the kicked rotor occurs near $K = 1$), becomes unstable again as it drops below ~ -1 , and so on. The phase space in Fig. 4.4(b) corresponds closely to the situation in our experiments, and from this plot it is apparent that the momentum boundary occurs well outside the range of $|p/2\hbar k_L| < 80$ that we measure experimentally. More details about this momentum boundary and its effects on quantum transport can be found in [Klappauf98b; Klappauf99].

4.5 Quantum Transport

Now we turn to the subject of quantum transport in the kicked rotor. We introduced in Chapter 1 the dynamical localization phenomenon, where the quantum transport is in sharp contrast with the diffusive classical transport. The main symptom of dynamical localization is that momentum

transport is frozen after the break time t_B . The underlying discrete-spectrum nature of the quantum dynamics also makes the quantum system numerically reversible, and hence manifestly nonchaotic, as we have also seen. In this section, we will examine several aspects of quantum transport in the kicked rotor, including some of the effects of noise on the quantum transport, and relate quantum and classical transport via their respective correlations.

4.5.1 Quantum Mapping

The equation of motion for the quantum δ -kicked rotor is just the Schrödinger equation,

$$i\hbar\partial_t|\psi\rangle = H|\psi\rangle , \quad (4.37)$$

where the Hamiltonian is given by Eq. (4.11). To derive a mapping for the quantum evolution, we start with the time-evolution operator $U(t, t_0)$ (so that $|\psi(t)\rangle = U(t, t_0)|\psi(t_0)\rangle$) for a system with a time-dependent Hamiltonian [Berestetskii71],

$$U(t, t_0) = \mathcal{T} \exp \left[-\frac{i}{\hbar} \int_{t_0}^t H(t') dt' \right] , \quad (4.38)$$

where \mathcal{T} is the chronological (time-ordering) operator, which is necessary when $H(t)$ does not commute with itself at different times. Using a procedure similar to that used in the derivation of the classical standard map, we can write the kicked-rotor evolution operator as

$$U(n+1, n) = \exp \left(-\frac{ip^2}{2\hbar} \right) \exp \left(-\frac{iK \cos x}{\hbar} \right) , \quad (4.39)$$

where the “kick” operator acts on the state vector first, followed by the “drift” operator.

The quantum mapping in the form (4.39) is particularly suitable for calculations, because each component of the operator is diagonal in either the x or p representation, and thus is simple to apply to the wave function after appropriate Fourier transforms. Alternately, we can express the quantum mapping entirely in the momentum basis by using the generating function for the Bessel functions $J_n(x)$, with the result

$$\psi_{n+1}(p) = \exp \left(-\frac{ip^2}{2\hbar} \right) \sum_{l=-\infty}^{\infty} i^l J_l(K/\hbar) \psi_n(p - l\hbar) , \quad (4.40)$$

where $\psi_n(p)$ is the wave function in the momentum representation just before the n th kick. The ladder structure in momentum space is once again apparent in this form of the mapping. Also, since $J_n(x)$ drops off exponentially with n for $n > x$, each kick couples any given state to about $2K/\hbar$ other states.

Because the Hamiltonian for the kicked rotor is explicitly time-dependent, the energy is not a constant of the motion, and therefore there are no stationary states for the system. However, since the Hamiltonian is time periodic, we can define temporal *Floquet states* (or *quasienergy states*), in analogy with the spatial Floquet/Bloch solutions for the eigenstates of a periodic potential that we discussed in Chapter 2. We can write these states in an arbitrary representation as

$$\psi_\epsilon(t) = e^{-i\epsilon t/\hbar} u_\epsilon(t) , \quad (4.41)$$

where $u_\epsilon(t)$ is a periodic function of time (with the same unit period as the scaled Hamiltonian), and ϵ is the quasienergy of the state. These states are eigenstates of the one-period evolution operator,

$$U(n+1, n)\psi_\epsilon = e^{-i\epsilon/\hbar}\psi_\epsilon , \quad (4.42)$$

and thus are eigenstates in a stroboscopic sense, since their probability distribution is invariant under one period of time evolution.

Before continuing with the discussion of the quantum kicked rotor dynamics, it is useful to consider one more form for the quantum evolution equations. In the Heisenberg representation, we can integrate the Heisenberg equation of motion for the operators to obtain a map for the operators x_n and p_n just before the n th kick:

$$\begin{aligned} p_{n+1} &= p_n + K \sin x_n \\ x_{n+1} &= x_n + p_{n+1} . \end{aligned} \quad (4.43)$$

This Heisenberg map has exactly the same form as the classical standard map (4.17), but with the classical variables replaced by quantum operators. What may seem surprising at first is that there is no mention of the quantum parameter \hbar . On iteration of the map, the sin function will operate on combinations of x and p , generating products of these operators at all orders, and thus Planck's constant enters via the commutation relation $[x, p] = i\hbar$. As we argued in Chapter 1,

then, it is the nonlinearity that brings about quantum deviations from the classical behavior, and we also expect quantum effects to show up after repeated iterations of the map, rather than after a single time step.

4.5.2 Dynamical Localization

The work of Fishman, Grempel, and Prange (FGP) [Fishman82; Grempel84; Fishman96] marked an important milestone in the understanding of quantum localization. In this work, FGP showed that the quantum mapping for the kicked rotor could be written in a form that suggests a strong analogy with the problem of Anderson localization in one dimension [Anderson58; Fishman96]. The Anderson problem considers the transport of an electron in a disordered potential, which consists of an array of barriers with flat regions between. The barriers are characterized by transmission and reflection probabilities, and classical particles that obey these particles would diffuse spatially throughout the potential. In the quantum case, if the barriers are arranged in a periodic fashion, there are certain particle energies that permit ballistic motion through the lattice (corresponding to the Bloch states of the system). This transport is analogous to the quantum resonance in the kicked rotor, to which we will return in Section 4.5.3. If the barriers are disordered, though, there is no resonance condition for long-range transport. In a path-summation picture [Feynman65], there are many paths by which an electron can travel to a distant site, but as a result of the disorder, the paths have random phases with respect to each other and thus tend to destructively interfere, effectively suppressing the quantum propagator for long-range transitions. The eigenfunctions in the Anderson problem are known to be exponentially localized, as opposed to the extended Bloch states. Additionally, FGP argued that although the kicked rotor has a dense point spectrum, the quasienergy spectrum is *locally* discrete in the sense that a localized excitation in momentum leads to a discrete spectrum, as states close together in quasienergy correspond to states that are widely separated in momentum [Grempel84].

In the Anderson-like form of the kicked rotor, the discrete “sites” are the plane-wave states in a momentum ladder, which are coupled by the kicks. The diagonal matrix elements that describe the lattice-site energies are pseudorandom [Fishman96] if $\hbar/2\pi$ is an irrational num-

ber (the rational case corresponds to the quantum-resonance phenomenon). In a more direct picture, the free phase evolution $\exp(-ip^2/2)$ between each kick causes the momentum-state phases to “twist,” and the phases of widely separated momentum states become effectively randomized by this part of the evolution for generic values of k . This pseudorandomness has essentially the same effect as the disorder in the Anderson problem, and thus the kicked-rotor Floquet states are likewise exponentially localized. This result provides a useful context for understanding dynamical localization, since the evolution to a localized state can be viewed as a dephasing of the quasienergy states. An initial momentum distribution that is narrow compared to a typical quasienergy state must be a coherent superposition of Floquet states. As time progresses, the precession of the phases of the basis states (each with different quasienergy) results in diffusive behavior for short times. At long times, when the basis states have completely dephased, the distribution relaxes to an incoherent sum of the exponentially localized basis states, resulting in an exponentially localized momentum distribution. For very long times, one also expects quantum recurrences as the basis states rephase [Hogg82], but these timescales are far beyond what we can observe experimentally.

An experimental measurement of dynamical localization is shown in Fig. 4.5. This plot shows essentially the picture at which we just arrived: the initially narrow momentum distribution relaxes after a short time into a nearly stationary, exponential profile. The shapes of the distributions at various times are shown more clearly in Fig. 4.6. In this semilog plot, the exponential tails of the distribution at late times appear as straight lines. In viewing these measurements, it is important to realize that this localization is indeed dynamical localization and not the less interesting “adiabatic localization” [Fishman96], which is a result of the momentum boundary that we described above, and is a classical effect. The clean exponential tails that we observe make it clear that the dominant effect is dynamical localization, as adiabatic localization is characterized by more sharply truncated tails at the momentum boundaries [Klappauf98c; Klappauf99].

The analysis that revealed the exponential nature of dynamical localization has implicitly assumed a kicked rotor, not a kicked particle. Since the continuous momentum space of the particle consists of many discrete, uncoupled, rotor-like momentum ladders, the same ar-

guments apply to each ladder separately, and we expect localization to occur in a similar way in the experiment. In fact, if the momentum distribution is coarse-grained on the scale of $\hbar k$, the particle momentum distribution evolves to a much smoother exponential profile than the rotor, due to averaging over the many ladders.

4.5.3 Quantum Resonances

In the cases where $\hbar k/2\pi$ is a rational number, the motion is of quite a different (but still distinctly nonclassical) character. To illustrate the effect here, we consider the case of $\hbar k = 4\pi$, and we restrict our attention to the “symmetric” momentum ladder, $p = s\hbar k$ for integer s (i.e., we are assuming a kicked rotor, rather than a particle). The kinetic energy part of the evolution operator

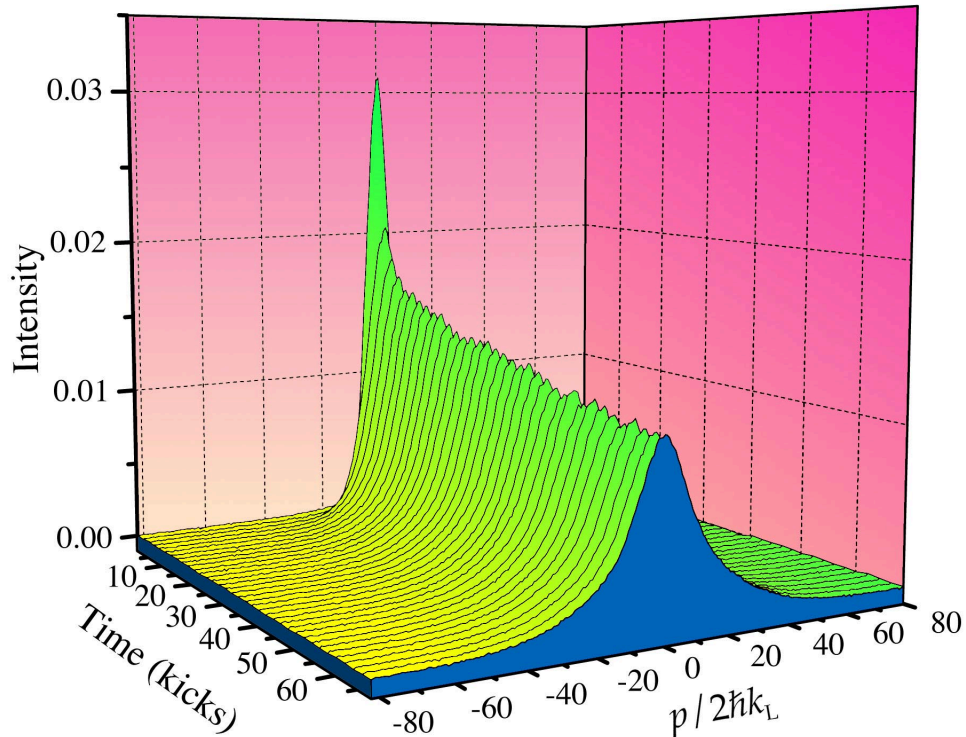


Figure 4.5: Experimental measurement of the momentum-distribution evolution in the kicked rotor, showing dynamical localization. Here $K = 11.5 \pm 10\%$, $T = 20 \mu\text{s}$ ($\hbar k = 2.077$), and $t_p = 0.283 \mu\text{s}$. The nearly Gaussian initial distribution ($\sigma_p/2\hbar k_L = 4.4$) relaxes rapidly to an exponential profile, which expands slowly.

from (4.39),

$$\exp\left(-\frac{is^2\hbar}{2}\right), \quad (4.44)$$

collapses to unity, and the evolution operator for n kicks can be written as

$$\exp\left(-\frac{inK \cos x}{\hbar}\right). \quad (4.45)$$

This operator is equivalent to the operator for a single super-kick with stochasticity parameter nK . Recalling the analysis based on the expanded form (4.40) of the quantum standard map, the wave packet in this case will have propagating edges (asymptotically) at $p = \pm nK$. Correspondingly, the kinetic energy increases as t^2 , which is characteristic of ballistic transport. This phenomenon is known as a quantum resonance [Izrailev79; Izrailev80], and is related to the Talbot effect in wave optics [Berry99].

The situation is obviously more complicated for the kicked-particle case, since the evolution operator does not trivially collapse for the other momentum ladders. The other states do not exhibit ballistic transport, but rather form a localized, Gaussian-like profile, which is narrower than the corresponding exponentially localized case [Moore95]. An analytic treatment of

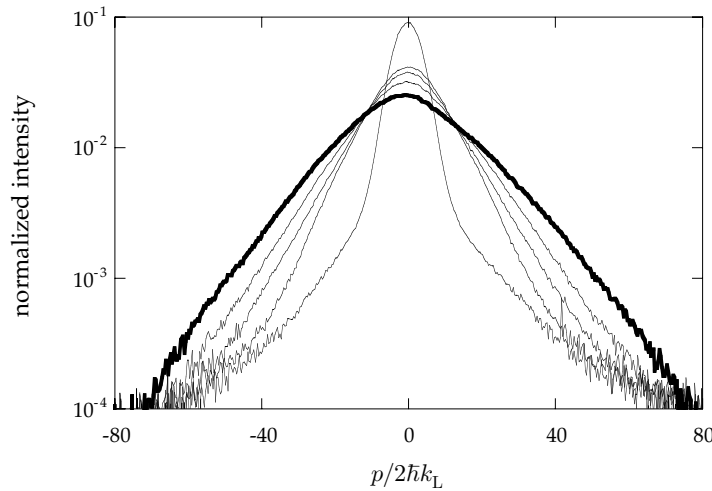


Figure 4.6: Experimentally measured momentum distribution evolution, shown for 0, 10, 20, 40, and 80 kicks ($K = 11.2 \pm 10\%$, $\hbar = 2.077$); the zero-kick case is the narrowest distribution, and the 80-kick distribution is highlighted in bold. Because the vertical axis in this plot is logarithmic, the tails of the localized (exponential) distribution appear as straight lines.

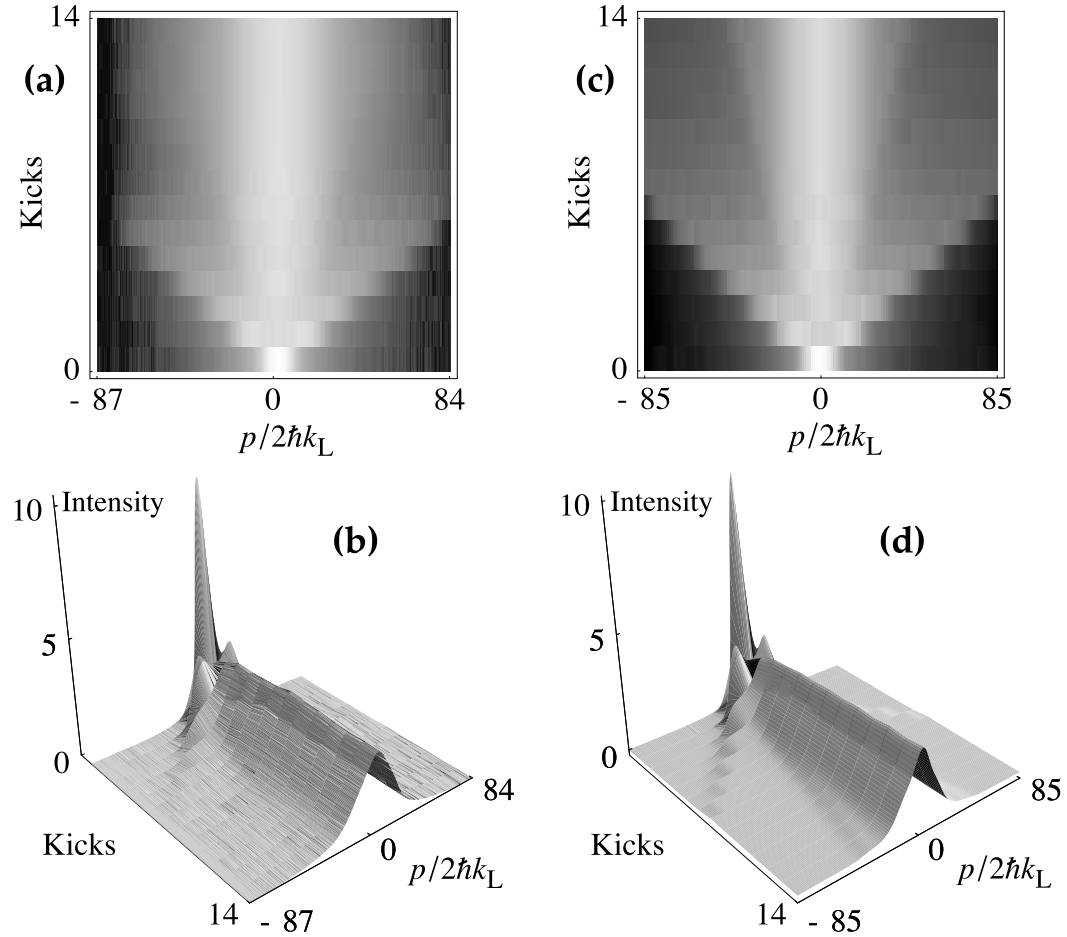


Figure 4.7: Experimental observation of ballistic transport at quantum resonance. The evolution of the atomic momentum distribution is plotted for the experimental measurement (a, b) and quantum simulation (c, d). The parameters are $\hbar k = 4\pi$ ($T = 121 \mu s$) and $K = 184$. The simulation assumed square pulses with $t_p = 0.295$ ns, and used an initial condition constructed directly from the experimentally measured initial distribution. In order to obtain good qualitative agreement and avoid numerical artifacts, a large simulation (that averaged over an ensemble of 50 wave packets, with centers distributed uniformly in position, and employed a grid spanning $p/2\hbar k_L = \pm 256$ with a resolution of $\Delta p/2\hbar k_L = 1/1024$, binned over $2\hbar k_L$ for a smooth distribution) was necessary.

the transport in this more general case can be found in [Bharucha99]. The coexisting ballistic and localized behaviors at the $\hbar = 4\pi$ quantum resonance are visible in the measured and simulated evolutions in Fig. 4.7.

Experimentally, only the low-order quantum resonances (with \hbar an integer or half-integer multiple of 2π) cause visible deviations from localization, as the higher-order resonances can take extremely long times to become manifest. The other low-order case that we have studied is the “antiresonance” at $\hbar = 2\pi$. For the symmetric momentum ladder, the kinetic-energy part of the evolution operator collapses to $(-1)^s$ for the state $p = s\hbar$, which effectively amounts to a time-reversal operator ($p \rightarrow -p$). In this case, an initial state on this ladder reconstructs itself every other kick. In the general particle case, the behavior is similar to that of the $\hbar = 4\pi$ resonance [Oskay00].

4.5.4 Delocalization

We now turn to the concept of the destruction of localization in the quantum kicked rotor. As the deviation from the classical dynamics is primarily a result of long-time quantum correlations, dynamical localization should be susceptible to external noise and environmental interaction, either of which would suppress these correlations. Note that noise and environmental interaction are fundamentally different in nature: noise is a unitary process, and is hence reversible in principle, whereas the latter case is an interaction with a very large (i.e., possessing many degrees of freedom) external system (reservoir), which is an inherently irreversible process. However, a noisy (stochastic) perturbation is the important effect of the environment, as we argued in Chapter 1, so that from an experimental point of view, these two situations are effectively equivalent. For the quantitative study of delocalization in Section 4.6, we chose to study noise effects because of the high degree of experimental control over the noise implementation. The first theoretical study of the influence of noise on the quantum kicked rotor appeared in [Shepelyansky83], where it was found that a sufficiently strong random perturbation could restore diffusion at the classical rate. Soon thereafter, a more detailed theoretical treatment was presented by Ott, Antonsen, and Hanson [Ott84], who showed that if the scaled Planck constant

is sufficiently small, classical diffusion is restored, even for small amounts of added noise.

In the heuristic picture presented in [Fishman96], the noise can be characterized by a coherence time t_c , beyond which quantum coherence is destroyed. In the case of weak noise, where $t_c \gg t_B$, the noise restores diffusion after the break time at a rate proportional to $1/t_c$, which is much slower than the initial classical-like diffusion phase. If, on the other hand, the coherence time is less than the break time, then we expect (for small \hbar) that localization is completely destroyed and classical behavior is restored.

We will now examine experimental evidence that localization can be destroyed by interaction with optical molasses. This situation is effectively an interaction with a dissipative environment, which causes momentum perturbations due to the photon absorption and emission and also dissipation of kinetic energy due to the cooling effect of the molasses. The effect on the kinetic energy evolution is plotted in Fig. 4.8 for several different values of the spontaneous scattering rate. Qualitatively, the energy diffusion increases with increasing scattering rate. This increased heating cannot be explained in terms of trivial photon-recoil heating be-

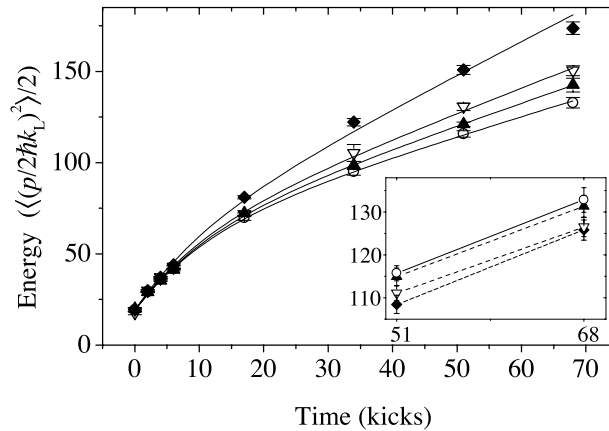


Figure 4.8: Experimental observation of decoherence due to spontaneous photon scattering in optical molasses. The scattering probabilities are 0% (circles), 1.2% (filled triangles), 5.0% (open triangles), and 13% (diamonds) per kick, and the kicked-rotor parameters are $K = 11.9 \pm 10\%$ and $\hbar k = 2.077$. Although spontaneous emission generally causes momentum diffusion and therefore heating of the atomic sample, the optical molasses cools the atoms, as shown in the inset, where the molasses interaction was added *after* the lattice kicks. Thus, the enhanced diffusion in this dissipative case is due only to the destruction of localization.

cause the molasses cools the distribution, and so the increased heating indicates the destruction of localization. The corresponding effect of the molasses light on the momentum distribution evolution is shown in Fig. 4.9. The exponential profile is again evident in the zero-noise case. As the spontaneous emission is applied, the late-time distribution becomes rounder, taking on a Gaussian profile in the cases of 5.3% and 13% scattering probability per kick (this seems to disagree with [Doherty00], where it is claimed that the distributions remain “essentially exponential” with scattering rates around 5%/kick).

The reader may notice in Fig. 4.8 that the late-time energy growth in the zero-noise case, while slower than the short-time growth, is still nonzero, as we might expect from a simple picture of localization. However, “perfect” localization is not necessarily expected over the time scales considered in the experiment, as we can see from the quantum simulation in Fig. 1.5.

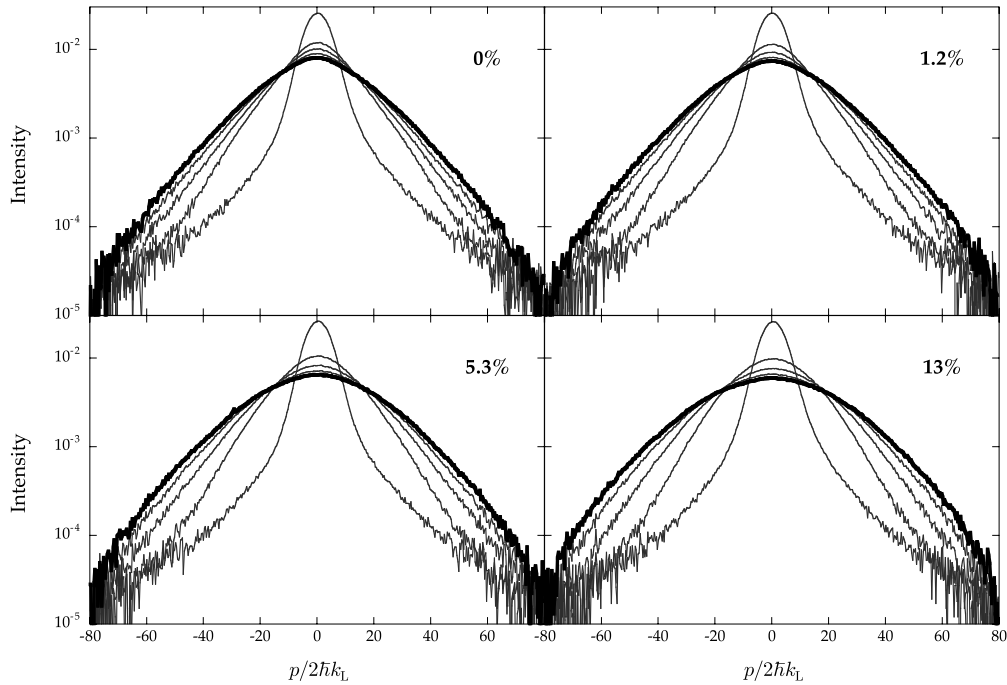


Figure 4.9: Experimental study of how the dissipative optical molasses interaction influences the momentum distributions in the quantum kicked rotor. The scattering rates here, 0%, 1.2%, 5.3%, and 13%, correspond closely to those displayed in Fig. 4.8. At the higher scattering rates, the late-time distribution makes a transition from the localized exponential profile to a classical-like Gaussian shape (which appears parabolic in these semilog plots).

We have verified that this late-time growth is not due to the nonideal effects of the optical lattice discussed in Chapter 2 by varying the lattice detuning while keeping V_0 constant by compensating with a corresponding lattice intensity change. The other sources of noise are small, but it is difficult to rule out residual phase noise of the lattice (caused by mechanical vibrations of the retroreflecting mirror) as a contribution to late-time diffusion. (Recall that we have characterized the phase noise in the optical lattice in Section 3.4.2).

We have also studied the effects of amplitude noise in the quantum kicked rotor (we examine these results in Section 4.6), as well as noise in the time between kicks and spontaneous emission from a far-detuned traveling wave applied between kicks. All of these noises cause a similar transition from localization to classical-like diffusion at late times. The different types of noise should in principle be different in nature. Amplitude noise is “ladder-preserving,” which means that atoms can still only change momentum by $2\hbar k_L$ at a time, even with this perturbation. Other types of noise, such as spontaneous emission, are “nonperturbative” in the sense that they can break this ladder symmetry. As a result of the interaction of the previously uncoupled ladders, this noise can lead to more effective destruction of localization [Cohen91; Fishman96; Cohen99]. A quantitative comparison between perturbative and non-perturbative noises is difficult, though, and we cannot distinguish any differences based on our current data. A clean quantitative study would probably best be accomplished with different types of noise than we have studied, which could be for example a perturbation by a second lattice with a different period [Cohen99] (realized by crossed but not counterpropagating laser beams).

4.5.5 Quantum Correlations

The above analysis leading to exponential quantum localization was based on dynamically generated disorder, and therefore we might expect that correlations also play an important role in the quantum dynamics. Shepelyansky showed numerically [Shepelyansky83] and analytically [Shepelyanskii82] that whereas the classical correlations drop off quickly with time (when any residual stable structures are too small to affect the dynamics on a short time scale, i.e., away

from the accelerator modes), the quantum correlations persisted for much longer times than the corresponding classical correlations. In contrast, for cases of smaller K (and hence more stability), the quantum and classical correlations were similar after the break time. This difference in the correlations is intuitively clear from Eq. (4.23). For localization, the long-time quantum correlations near the break time must be negative, bringing this sum to nearly zero, in order for the diffusion to freeze. For the quantum resonance case, the correlation series must have a long positive tail, such that the sum (4.23) diverges.

Shepelyansky also made another important observation regarding the quantum correlations, which will be important for the interpretation of the results presented here. In particular, he calculated the first few quantum correlations and found that they had approximately the same form as the corresponding classical correlations upon the substitution [Shepelyansky87; Shepelyanskii82; Cohen91]

$$K \longrightarrow K_q := \frac{\sin(\hbar/2)}{\hbar/2} K . \quad (4.46)$$

(Note, however, that the correlations used in [Shepelyansky87] were defined without the factor of K^2 that appears in Eq. (4.21).) Hence, a good approximation for the initial quantum diffusion rate in the absence of noise is

$$D_q(K, \hbar) = \frac{K^2}{2} \left(\frac{1}{2} - J_2(K_q) - J_1^2(K_q) + J_2^2(K_q) + J_3^2(K_q) \right) , \quad (4.47)$$

where, as in the classical calculation, it is assumed that the initial quantum distribution is uniform over the unit cell in the classical phase space. Consequently, there is an oscillatory dependence of the initial quantum diffusion rate on K_q that is closely related to the underlying classical dynamics. However, the oscillations are shifted due to the quantum scaling factor in (4.46). Since the width of the localized distribution (the *localization length*) is related to the initial diffusion rate by the heuristic/numerical result [Shepelyansky87; Fishman96],

$$t_B \approx \xi = \frac{D_q}{\hbar^2} \quad (4.48)$$

(where ξ is the localization length of the Floquet states, so that the momentum probability distributions have the form $\exp[-|p - p_0|/(\xi/2)]$), these oscillations are also apparent in the long-time quantum distributions.

This oscillatory structure and the confirmation of the quantum scaling is shown in Fig. 4.10, where the experimentally measured energy is plotted for a fixed interaction time as a function of K_q . The correct quantum scaling causes the oscillations in these curves to match for different \bar{k} . At the maxima of these curves, the late-time momentum distributions are not exponential, having more of a curved profile in the tails, as shown in Fig. 4.11. This effect is likely an influence of the accelerator modes and possibly other stable structures. Theoretical work has shown that classical anomalous transport enhances fluctuations in the Floquet-state localization lengths [Sundaram99a], and the deviations of the quasienergy states from a purely exponential shape may also be due to classical correlations [Satija99]. We will also return to this issue of the late-time distribution shape in Section 4.7.

Notice that to reach the classical limit in our experiment, the short-term correlations must also be modified by the noise. This is especially true in view of the shift caused by the quantum scaling factor in (4.46), which shifts the diffusion oscillations by about 20% in K for

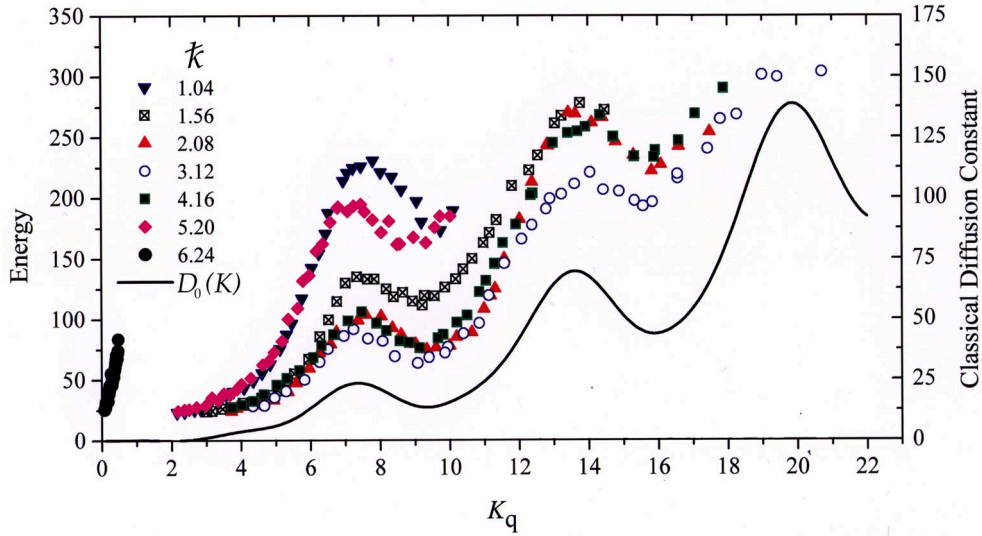


Figure 4.10: Experimental verification for the scaling of K_q . The measured ensemble kinetic energy is plotted for a fixed time as a function of the rescaled stochasticity parameter for several values of \bar{k} . The measurement times are 35 kicks ($\bar{k} = 1.04, 1.56, 2.08, 3.12, 4.16$), 28 kicks ($\bar{k} = 5.20$), and 24 kicks ($\bar{k} = 6.24$). The solid line is a plot of the classical (standard map) diffusion rate, Eq. (4.24). The locations of the oscillatory structures match well when plotted in terms of the rescaled K , supporting the validity of the K_q scaling.

the typical experimental value $\bar{k} = 2.08$ in the experiments here. It is possible to generalize the work of Shepelyansky leading to Eq. (4.47) to include amplitude noise in essentially the same way as in the classical calculation, with the result (see Section 4.8 for details)

$$D_q(K, \bar{k}) = \frac{K^2 + \text{Var}(\delta K)}{4} + \frac{K^2}{2} (-\mathcal{Q}_2(K_q) - \mathcal{Q}_1^2(K_q) + \mathcal{Q}_2^2(K_q) + \mathcal{Q}_3^2(K_q)), \quad (4.49)$$

where

$$\mathcal{Q}_n(K_q) := \int_{-\infty}^{\infty} P(\delta K) J_n(K_q + \delta K_q) d(\delta K), \quad (4.50)$$

and $\delta K_q = \delta K \sin(\bar{k}/2)/(\bar{k}/2)$. Thus, the short-time quantum correlations are washed out in much the same way as the classical correlations, as in Eq. (4.29). However, since the locations of the classical and quantum oscillations in $D(K)$ are different for our operating parameters, we can conclude that in order to observe good correspondence between quantum and classical evolution, the applied noise must be very strong (i.e., we must have t_c on the order of one kick, so that all the higher-order correlations are destroyed). In this case, both quantum and classical diffusion will proceed at the quasilinear rate, since the diffusion oscillations will be destroyed (as

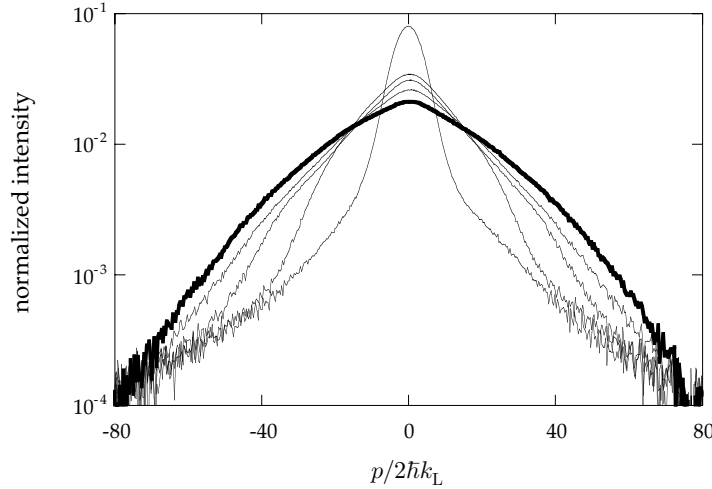


Figure 4.11: Experimentally measured momentum-distribution evolution, shown for 0, 10, 20, 40, and 80 kicks. In this plot, $K = 8.4 \pm 10\%$, $\bar{k} = 2.077$, corresponding to a peak in the quantum diffusion curve (as in Fig. 4.10). The zero-kick case is the narrowest distribution, and the 80-kick distribution is highlighted in bold. The late-time distribution is qualitatively different from the exponentially localized case in Fig. 4.6, which corresponds to a minimum in the quantum diffusion curve.

in Fig. 4.3), and the global behavior will be the same. For lower levels of noise, we might expect to recover diffusive behavior in the quantum system (if the long-time correlations responsible for localization are destroyed), but possibly at a rate that does not match the classical prediction. Heuristically, in the picture of [Ott84; Cohen91], the noise causes diffusion in momentum at a rate $2D$, and we can expect coherence to be broken when diffusion occurs on the scale $\hbar k$ between neighboring momentum states, so that

$$t_c = \frac{\hbar^2 k^2}{2D} . \quad (4.51)$$

For the case of uniformly distributed amplitude noise, this estimate becomes

$$t_c = \frac{24\hbar^2 k^2}{(\delta K_{p-p})^2} . \quad (4.52)$$

We can insert some values corresponding to the data to be analyzed in Section 4.6.2.1, where $K = 11.2$ and $\hbar k = 2.08$. In order to break localization, we must have $t_c \sim t_B$, which is around 10 kicks in the experimental data, thus requiring about 30% amplitude noise. To obtain good correspondence, however, requires $t_c \sim 1$ for quasilinear diffusion, and thus the higher noise value of around 90%. These simple estimates are in reasonable agreement with the experimental data.

4.6 Quantitative Study of Delocalization

Up to this point, we have shown that noise can lead to a loss of localization, with distributions that have a classical form. However, we have not yet addressed the more interesting question of whether the experimental data match the classical prediction in the presence of noise. Answering this question in a quantitative way requires a nontrivial amount of effort in carefully modeling the experiment in order to make an accurate classical prediction for comparison with the experimental data.

4.6.1 Classical Model of the Experiment

In order to facilitate an accurate comparison of the experimental data to the classical limit of the kicked rotor, we have performed classical Monte Carlo simulations of the experiment. In

these simulations, a large number (2×10^5) of classical trajectories were computed, each with a distinct realization of amplitude noise; momentum distributions and ensemble energies were then extracted from this set of trajectories. Additionally, we accounted for several different systematic effects that were present in our experiment, in order to provide the best possible classical baseline for comparison with the experimental data. In the remainder of this section we describe in detail each of the systematic effects that we have accounted for and how we have included them in the comparison of the data to theory.

The effects that we will describe in this section are illustrated in Fig. 4.12. This plot compares the energy evolution for different cases where different corrections are accounted for. As each correction is (cumulatively) taken into account, the resulting energy curve is lower and less linear. Indeed, there is quite a large difference between the uncorrected, linear δ -kick curve that one might expect to observe and the fully corrected curve. The importance of this rather

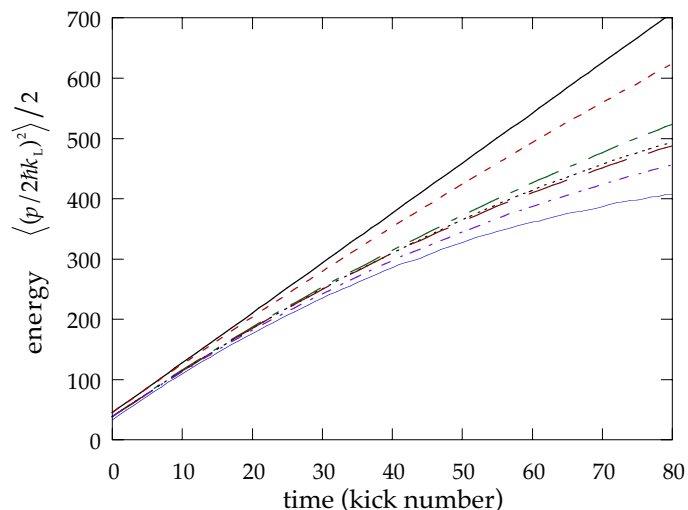


Figure 4.12: Example of how the systematic effects described in the text can affect the measured energies. Shown are the simulated average energy evolution for typical operating parameters ($K = 11.2$, 100% noise level) and typical parameters for the systematic corrections. The solid curve is the ideal case, corresponding to the δ -kicked rotor with no corrections; the successively lower curves represent the cumulative result as each effect is accounted for (in the order of presentation in the text): nonzero pulse duration (dashed), MOT (detection) beam profile (long dot-dash), clipping due to width of CCD chip (dotted), profile of interaction beam/transverse atomic motion (long dashes), correction for free-expansion measurement (dot-dash), and vertical-offset bias (thin solid).

technical discussion of experimental details is clear: without carefully taking into account these systematic effects, one might mistakenly attribute curvature in the experimental energy data to residual quantum localization effects. It is also important to emphasize that these effects cause a reduction in the dynamic range of the experimental measurements, but they do not change the underlying physics in a fundamental way. Finally, we note that most of these systematic effects are such that it is either impractical or impossible to compensate for them with a simple correction to the experimental data. In this sense, the “energies” that we use in our comparisons are not true energies, but relatively complicated functions of the true energies and many other experimental parameters. It is therefore the ability to take these effects into account in the classical simulations that allows for a meaningful quantitative comparison between our experiment and classical theory.

The first, and perhaps most important, effect that we account for is the detailed pulse shape $f(t)$ of our kicks. The nonzero temporal width of the pulses leads to an effective reduction in the kick strength at higher momenta, as we discussed in Section 4.4.4, and so it is important to accurately model the experimental pulses in order to reproduce the correct tails in the momentum distributions. It turns out that our experimental pulses are well modeled by the function

$$f(t) = \frac{1}{2\eta_{\text{erf}}} \left[\text{erf} \left(\frac{(t - t_1)\sqrt{\pi}}{\delta t_1} \right) - \text{erf} \left(\frac{(t - t_2)\sqrt{\pi}}{\delta t_2} \right) \right], \quad (4.53)$$

where $t_2 - t_1 = 295$ ns is the full width at half maximum (FWHM) of the pulse, $\delta t_1 = 67$ ns is the rise time of the pulse (defined such that a straight line going from 0 to 100% of the pulse height in time δt_1 matches the slope of the rising edge at the half-maximum point), $\delta t_2 = 72$ ns,

$$\text{erf}(x) := \frac{2}{\sqrt{\pi}} \int_0^x \exp(-t^2) dt \quad (4.54)$$

is the error function, and η_{erf} is a normalization factor, which takes the value $t_2 - t_1$ for small values of $\delta t_{1,2}/(t_2 - t_1)$. The function (4.53) is plotted along with a measured optical pulse in Fig. 4.13. The rise and fall times in the pulse were mainly due to the response time of the switching AOM for the Ti:sapphire laser beam and the rise time of the SRS DS345 arbitrary-waveform synthesizer that drives the AOM controller. It should be noted that although the agreement between the pulse model and the experimentally measured pulses is excellent, Eq. (4.53) is merely

an empirical model of our observed pulse profiles. In the simulations, the classical equations of motion were directly integrated, using Eq. (4.53) for the kick profile.

The next effect that we consider is due to the Gaussian profile of the optical molasses laser beams. Recall that to measure momentum distributions, we imaged the light scattered by the atoms from the molasses beams after a free-expansion time. Since the light was not uniform over the atomic cloud, the scattering rate due to atoms with momentum p is given by

$$R_{\text{sc}} = N(p) \left(\frac{\Gamma}{2} \right) \frac{(I(x)/I_{\text{sat}})}{1 + 4(\Delta/\Gamma)^2 + (I(x)/I_{\text{sat}})} , \quad (4.55)$$

where $N(p)$ is the number density of atoms with momentum p , $I(x)$ is the local intensity at spatial position x , Γ is the excited state decay rate, and I_{sat} is the saturation intensity ($= 2.70 \text{ mW/cm}^2$ for approximately isotropic pumping on the trapping transition). Also, in the free expansion measurement, the unscaled variables x and p are related by

$$x = v_r(p/\hbar k_L)t_{\text{drift}} , \quad (4.56)$$

where $v_r = 3.5 \text{ mm/s}$ is the velocity corresponding to a single photon recoil, and t_{drift} is the free drift time of the momentum measurement. The spatial intensity profile of the six beams is

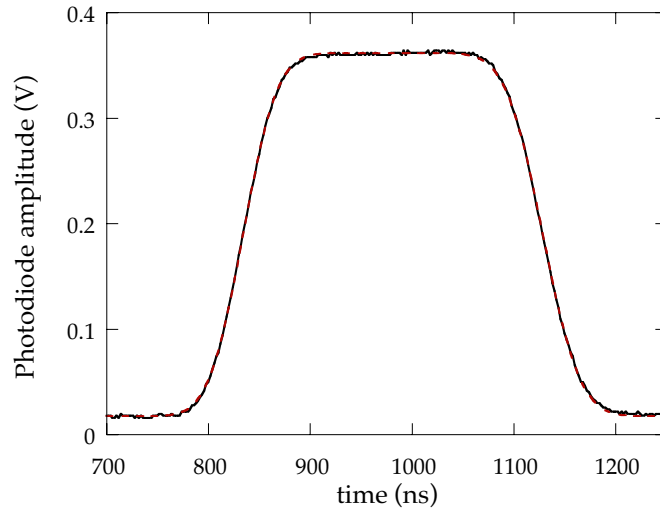


Figure 4.13: Model function (4.53) for the experimental pulses (dashed line) compared to an actual experimental pulse as measured on a fast photodiode (solid line). The two curves are nearly indistinguishable.

given by

$$I(x) = 2I_0 \left[e^{-2x^2/w_0^2} + 2e^{-(x^2+2z^2)/w_0^2} \right], \quad (4.57)$$

where I_0 is the intensity at the center of one of the six beams, $w_0 = 11$ mm is the beam-radius parameter of the Gaussian beams, z is the vertical position of the atoms (transverse to the standing wave, in the direction of gravity), the first term represents the two vertical beams, and the last term represents the four horizontal beams, each at 45° to and in the horizontal plane with the standing wave. To account for this effect, we applied a correction to the classical simulation of the form

$$f_{\text{mol}}(x) = \frac{f_1(x)}{c_2 + f_1(x)}, \quad (4.58)$$

where $f_1(x) = I(x)/2I_0$ is a scaled intensity profile, and $c_2 = [1 + 4(\Delta/\Gamma)^2][I_{\text{sat}}/(2I_0)]$. The value of c_2 was determined to be 5.94 by fitting the correction (4.58) to a known exponentially localized distribution for various drift times; this value is in reasonable agreement with the expected value of c_2 from the laser parameters.

The finite extent of our imaging CCD camera chip also had an impact on our measurements. We set up our imaging system such that a typical localized distribution was just contained within the imaged area after a 15 ms drift. For strongly noise-driven cases, though, the momentum distribution could extend significantly past the edges of the imaged area. This effect had little impact on the measured momentum distributions, since it only restricted the measurable range of momentum. However, the energies computed from this momentum distribution are sensitive to this truncation, even if the population in the truncated wings is small. The result is a systematic reduction in the measured energy. It was straightforward to model this effect in the simulations by rejecting trajectories that fall outside the experimental window.

Another effect that we accounted for is the transverse position of the atoms in the standing-wave beams. Although the spatial size of the beam (with $1/e^2$ radius $w_0 = 1.5$ mm) was large compared to the size of the initial MOT cloud ($\sigma_x = 0.15$ mm), the variation in kick strength over the atomic distribution must be accounted for, especially as the evolution progresses and the atoms move further out transversely. Hence each atom sees an effective kick

strength of $K_{\max} \exp[2(y(t)^2 + z(t)^2)/w_0^2]$, where the transverse coordinates y and z are given in scaled units by

$$\begin{aligned} y(t) &= y_0 + p_{y0}t \\ z(t) &= z_0 + p_{z0}t - gt^2/2 . \end{aligned} \quad (4.59)$$

In these equations, we have used the scaled gravitational acceleration g , which is related to the acceleration in physical units by $g = 2k_L T^2 g_{\text{phys}}$. In the simulations, each particle was given initial transverse positions y_0 and z_0 according to a Gaussian distribution that matched the measured MOT size, and initial momenta p_{y0} and p_{z0} that matched the momentum distribution measured along the standing wave. It should be noted that this correction may actually increase or decrease the final energies compared to an uncorrected simulation using the mean value of K , even though the mean value of K effectively decreases with time. This is because a subset of the atoms may completely dominate the diffusion if they are located more closely to one of the maxima of $D(K)$. For the beam waist/MOT size ratio used here, there is a spread in K of around 5% in our initial distribution.

We additionally accounted for a systematic effect that occurred in our free-expansion measurement technique. This technique relied on allowing the atomic cloud to expand freely for 15 ms after the interaction with the standing wave in order to convert the spatial distribution of the atoms into an effective momentum distribution. However, the interaction with the standing wave lasted as long as 1.6 ms for these experiments. Since we define the drift time as the time from the beginning of the standing-wave interaction to the beginning of the camera exposure, the drift time effectively becomes smaller as the number of kicks in the experiment increases. There is no simple way to directly correct for this effect, so we included this effect in our simulations by simulating the free-expansion process. The initial spatial distribution was chosen (in scaled units) to be uniform in the range $[-\pi, \pi)$, which is extremely small compared to the spatial distribution after the expansion. We did not choose the distribution from the MOT spatial distribution to account for convolution effects; these effects have been approximately accounted for already, since the initial momentum distribution used in the simulations is the measured momentum distribution, which was already convolved with the initial spatial distribution. Then the effective momentum of each particle measured by the free-expansion

method is given by

$$p_{\text{eff}}(t) = x(t) + \left(\frac{t_{\text{drift}} - t}{t_{\text{drift}}} \right) p(t) , \quad (4.60)$$

where all quantities in this equation are scaled.

The final effect that we took into account was due to variations in the background levels measured by the data acquisition (Princeton Instruments) camera. Although we performed background subtraction, which greatly improved our signal-to-noise ratio, the offset levels after the subtraction were generally nonzero, due to fluctuations (from drifts in the camera electronics) and constant offsets (from physical effects in the imaging of the atomic cloud). To enhance the reproducibility of our data, we used the following procedure to fix the zero level of our measured distributions: the 40 lowest points (out of 510 total) in the distribution were averaged together and defined to be the zero level. The disadvantage of this technique is that it resulted in a slight negative bias in the offset level from the “true” distribution. For typical measurements of localized distributions, the bulk of the distribution was contained well within the imaged region. In these cases, the measured values near the edges of the imaged region were small compared to those in the center of the distribution, and the error in the offset was negligible. However, for strongly noise-driven cases, a significant fraction of the distribution could fall outside the imaged region, as noted above. In these cases, the lowest 40 values were then significantly different from the true zero level, and our procedure introduced a significant bias. It was straightforward to mimic this process in the simulations, but in some data sets it was possible to restore the correct offset level. For our typical studies of the transition from localized to delocalized behavior, the only cases that were significantly biased are the strongly noise-driven cases, which behaved essentially classically (as we will see later). Then one can assume that the biased cases can be modeled as Gaussian distributions, with the MOT beam profile correction applied to them, and obtain the correct offset by fitting the model function to the measured distribution. This *ansatz* was justified by the essentially perfect fit of the model function whenever its use was appropriate. Using this idea, we implemented an automatic procedure for restoring the correct offset in the data sets where the procedure was sensible (Figs. 4.15-4.20). In other data (Fig. 4.14), such as measurements of exponentially localized distributions with very

long localization lengths, such a procedure was clearly inappropriate, and this effect was instead accounted for in the corresponding simulations.

There are a few other effects that we did not account for in the simulations, including spontaneous emission, the stochastic dipole force, collisions between atoms, and other sources of noise, most notably phase jitter in the standing wave (we have discussed all these effects in more detail in Chapter 2). These effects cause decoherence, but they were sufficiently weak that at low levels of applied amplitude noise, quantum effects were easily observed, and at high amplitude noise levels, the applied noise dominated any effects that these other processes might have had. Thus, these effects did not hinder our ability to study quantum-classical correspondence in our system.

We also note that the corrections we have mentioned lend themselves well to classical Monte Carlo simulations, whereas with other methods it would be quite cumbersome to take the many aspects of the experiment into account. A similar, quantum-mechanical analysis is much more difficult, however, as one would need to average over many wave packets in a Monte Carlo approach to obtain good convergence, and the evolution for a single quantum wave packet requires much more computation than for a single classical particle.

4.6.2 Data and Results

In this section we will explore a detailed experimental study of the quantum kicked rotor dynamics in the presence of amplitude noise, using the classical model for comparison. An overview of these results appears in Fig. 4.14, where the energies from the experiment and classical model are shown as a function of the kick strength K , for four different levels of amplitude noise. The energies are plotted at the fixed time of 35 kicks. In the case of no applied noise, one can clearly see the oscillations that correspond to Eqs. (4.24) and (4.47). Additionally, the shift in the locations of the experimental oscillations from their classical counterparts is evident; for the value of $\hbar = 2.08$ used in all the experiments shown here, the shift is 20% above the classical value. Although in some locations the quantum (experimentally observed) energies are larger than the classical (numerically calculated) energies due to the shift of the oscillations, the experimen-

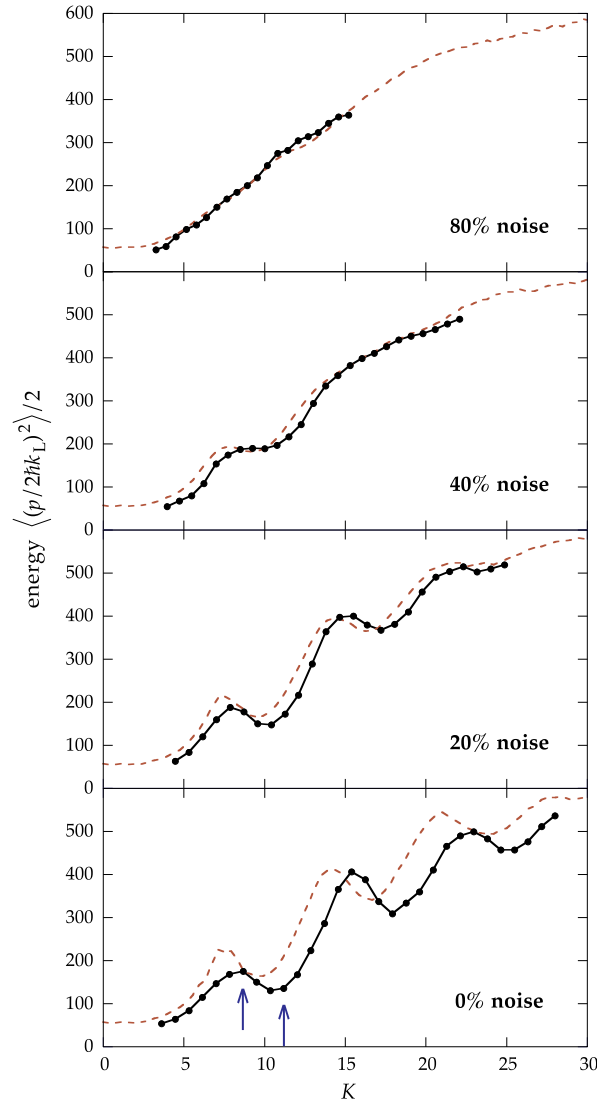


Figure 4.14: Plot of the experimentally measured energy (points connected by solid lines) and energy from the classical model (dashed line) as a function of the stochasticity parameter K , for several different levels of applied amplitude noise. All the plotted energies are measured at the fixed time of 35 kicks. The oscillations and the shift due to quantum effects, corresponding to Eqs. (4.24) and (4.47) with $\bar{k} = 2.08$, are evident in the case with no applied noise. On average, the experimental energies at the lower noise levels are smaller than their classical counterparts due to localization effects. However, for the strongest noise level shown here (80%), there is good agreement between the two energy curves. For this figure, no adjustments have been made to the measured values of K , and the error bars for the energy values are suppressed, but are typically smaller than the corresponding dots. Each experimental point is an average over 10 realizations of amplitude noise. Two arrows in the zero-noise case mark the locations of detailed study that are described in the following two subsections.

tal energies are smaller on average than the classical energies because of quantum localization effects.

As the noise is added, the oscillations in the energy curves become washed out, as one expects from Eqs. (4.29) and (4.49). Additionally, the difference between the experimental and classical curves becomes less apparent, until the highest noise level (80%), where there is excellent agreement between the two curves. In accordance with our previous discussion, good correspondence only occurs when the noise level is sufficiently large to destroy the short-time quantum and classical correlations, and hence the oscillations in the diffusion curves.

To fill out this picture of the kicked-rotor behavior, detailed views of the experimental and classical dynamics at two values of K appear below. The two values of K in these detailed measurements correspond to a minimum and a maximum of the quantum energy curve in Fig. 4.14; these locations are indicated as arrows in the zero-noise plot in this figure. As we mentioned above, the dynamics are qualitatively different at these two locations. At the minima of the experimental diffusion curve, exponential localization occurs. However, at the maxima, the late-time distributions that we measured in our experiment are nonexponential; this behavior is a fingerprint of the underlying classical anomalous diffusion.

In Figs. 4.15-4.20, we contrast the behavior of the experimental and classical systems at these two values of K . The behaviors at small noise levels have several interesting differences, but as we have already seen, the behavior at high noise levels is similar in that there is good correspondence between the experiment and the classical simulations. In Figs. 4.15 and 4.18, we see the behaviors of the energies at the minimum and maximum of the experimental diffusion curve, respectively, at a fixed time (50 kicks) as the level of noise varies. The time evolutions of the energies are shown in Figs. 4.16 and 4.19 for the two values of K at various levels of noise. Finally, the corresponding evolutions of the momentum distributions themselves are shown in Figs. 4.17 and 4.20. We will discuss these results for the two values of K separately in the following presentation.

Before proceeding, though, a few remarks are in order about the comparisons between the experiment and the corresponding classical dynamics performed in this paper. The classical

model contains many experimental parameters beyond the two that are really important for the quantum kicked rotor dynamics (K and \hbar). For the purposes of comparison, these extra parameters were not treated as fitting parameters; instead, they were all fixed to their experimentally measured values. However, the stochasticity parameter K , which is by far the largest source of uncertainty in the experiments, was sometimes adjusted by a few percent from its measured value (but well within the experimental uncertainty of $\pm 10\%$) in order to obtain better correspondence. To be precise about these adjustments, the measured values of K are quoted in each figure caption along with the value used in the classical simulations. Finally, as noted before, although statistical errors for our energy measurements are quoted in each figure, they are of limited utility in determining the quality of the correspondence between the experimental results and classical simulations. The main reason for this statement is the long-term optical alignment and laser drifts that result in long-term drifts in K , which can result in local systematic shifts in energies between different curves (or even points within a curve) in each figure. This effect is not properly accounted for by either the statistical error estimates or the simulations, which used a single value of K for an entire data set. For example, in Figs. 4.16 and 4.19, it is not possible to distinguish different levels of agreement between the data and simulations for the 60-200% noise levels, although some pairs of curves may appear to agree more closely than others. Indeed, it is important to realize that the momentum distributions are the most reliable tool for studying correspondence, since they contain much more information and tend to be less sensitive to the problems we have mentioned. The energies, on the other hand, are still valuable as a concise summary of the large amount of information presented here.

4.6.2.1 Detailed Study: Destruction of Exponential Localization

We now focus on the behavior at the minimum of the experimental diffusion curve, as indicated by the rightmost arrow in Fig. 4.14. In this regime, the atoms localize in an exponential distribution at late times. In Fig. 4.15, there is a large difference between the experimental and classical energies after 50 kicks when no noise is applied. This difference is due to both dynamical localization and the misalignment of the quantum and classical diffusion oscillations, which gives the classical system a larger initial diffusion rate. As noise is added, both the experimental data and

the classical simulations exhibit increased diffusion, as the short-time correlations are washed out. The increase in the experimental diffusion is larger than the classical diffusion because quantum localization is destroyed. At high noise levels, the agreement between experiment and classical simulation is good. Additionally, both curves exhibit a characteristic dip in the energy around 150% noise levels. This somewhat surprising effect is a result of residual short-time correlations, which persist at noise levels as high as 100%, where they enhance diffusion slightly above the quasilinear value.

Similar behavior occurs in the time evolution of the energies shown in Fig. 4.16. When there is no applied noise, the experimental energy grows initially more slowly than the classical energy, and then saturates and diffuses slowly. As we noted before, this slow diffusion may be due to residual decohering effects in our experiment, such as phase noise in the standing wave. As noise is added, the diffusion is enhanced in both cases, and for high noise levels the energy

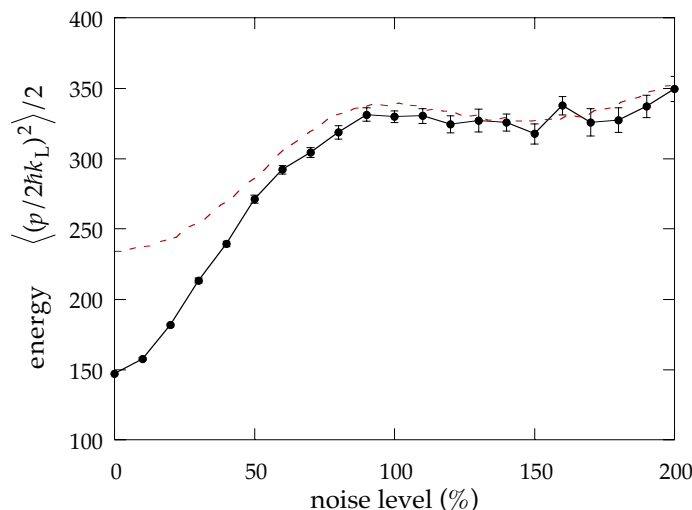


Figure 4.15: Experimentally measured energy (points and solid lines) and energy from the classical model (dashed line) as the noise level is changed, for a fixed time (50 kicks) and stochasticity parameter (the experimental value is $K = 11.2 \pm 10\%$, the classical simulation corresponds to $K = 10.9$). At the lowest noise levels, there is a significant difference between the experimental and classical energies, due to both localization and differences in short-term correlations, which disappears for high noise levels. The error bars represent statistical scatter among the 18 noise realizations comprised in each point, but do not account for long-term drifts or systematic uncertainties (see note in text). The value of K used here corresponds to the rightmost arrow in Fig. 4.14.

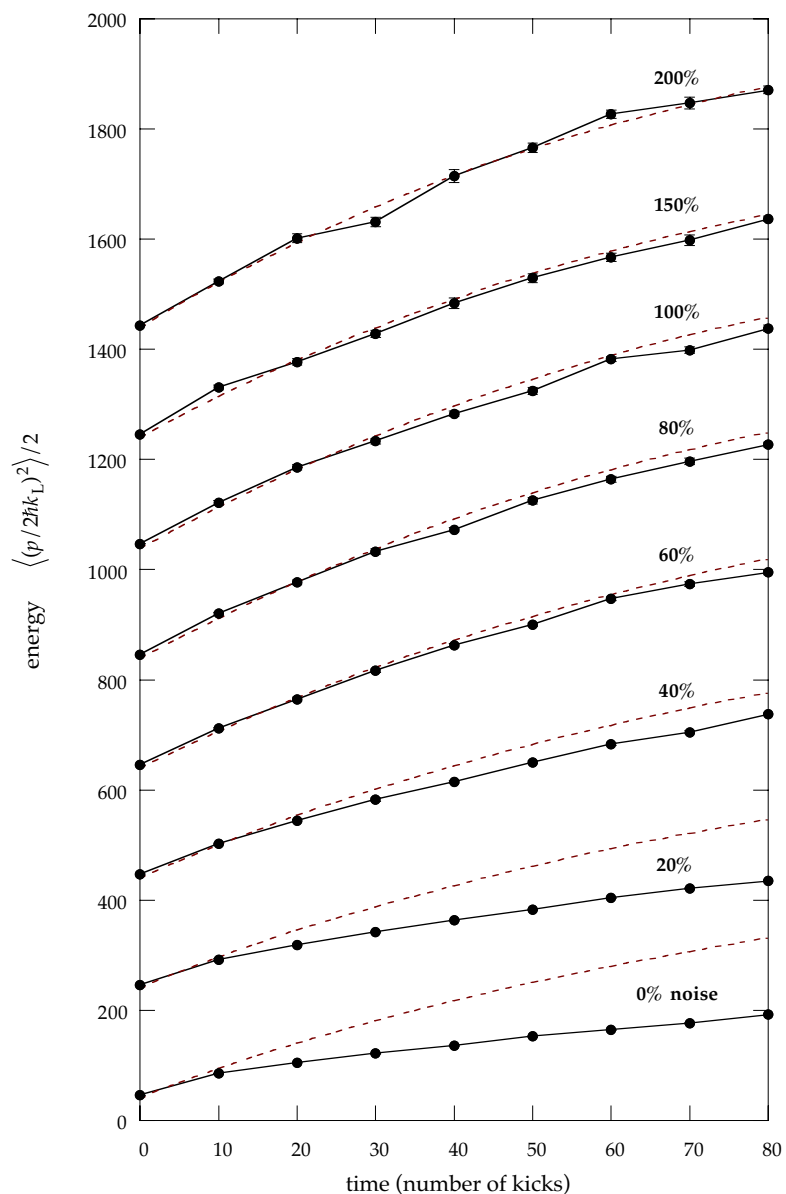


Figure 4.16: Experimentally measured energy (points and solid lines) and energy from the classical model (dashed line) as a function of time, for various levels of applied noise. The experimentally measured stochasticity parameter is $K = 11.2 \pm 10\%$, and the simulation corresponds to $K = 11.2$. The experimental data points are averages over 15 distinct realizations of amplitude noise, and data for successive noise levels are offset vertically by 200 for clarity. The agreement between the experimental data and the classical model is excellent for noise levels of 60% and above. The value of K used here corresponds to the rightmost arrow in Fig. 4.14.

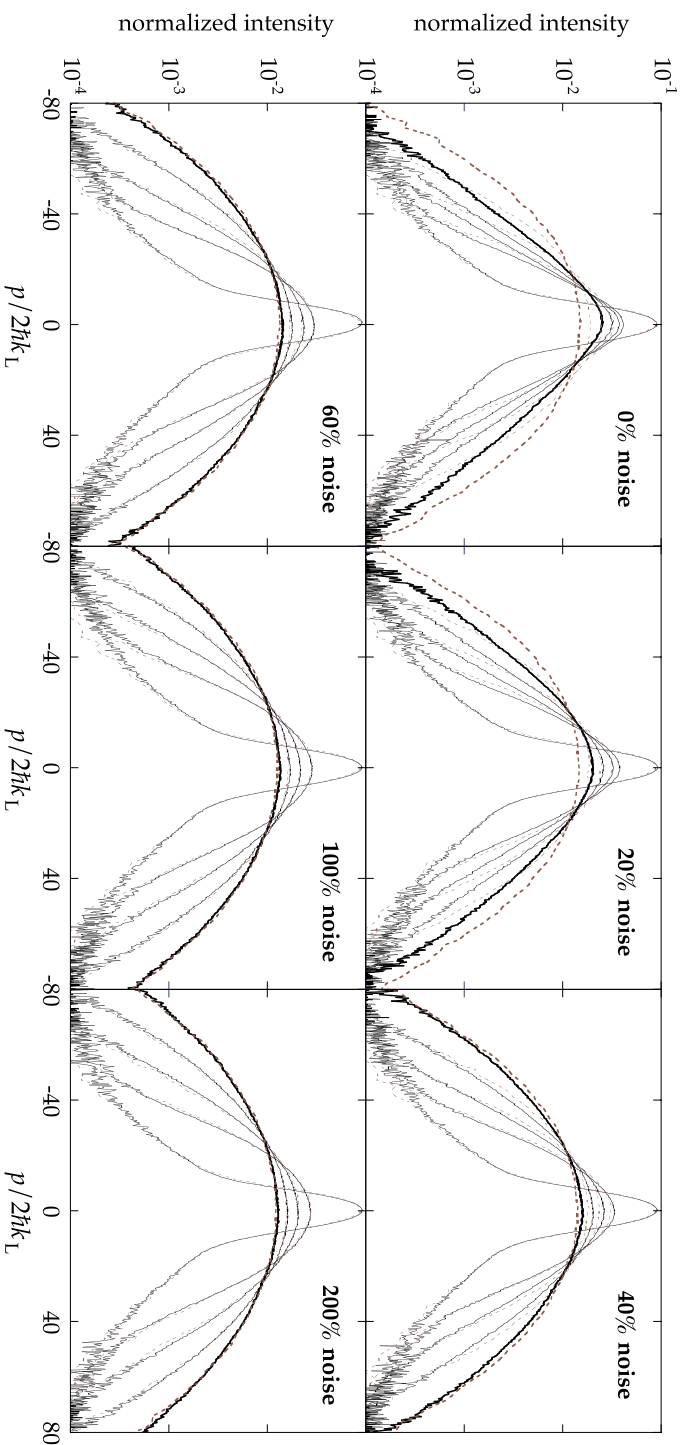


Figure 4.17: Evolution of the momentum distributions, for both the experiment (solid) and classical model (dashed), at various levels of applied noise. The experimentally measured stochasticity parameter is $K = 11.2 \pm 10\%$, and the simulation corresponds to $K = 11.2$. The times shown, in order of increasing width, are 0, 10, 20, 40, and 80 kicks, with the final distributions emphasized in bold. In the zero-noise case, the contrast between the exponentially localized experimental distribution and the classical Gaussian distribution is evident. For the largest three levels of noise shown, the experimental and classical distributions are nearly indistinguishable. The data and simulations presented in this figure are the same as those used to calculate the energies in Fig. 4.16, and the value of K used here corresponds to the rightmost arrow in Fig. 4.14 (the “valley” in the experimental curve).

growth in the experiment is quite similar to that observed in the simulations.

Finally, the transition to classical behavior in the experiment is most dramatically evident in the momentum distributions in Fig. 4.17. In the zero-noise case, the experimental distribution evolves from the initial, nearly Gaussian form to the exponentially localized distribution (shown in bold), which is characteristic of dynamical localization. The classical distribution, on the other hand, evolves to the broader, Gaussian distribution that one expects from classical physics. When a small amount of noise (20%) is applied, the final experimental distribution is broader and has a rounded appearance, but is still quite far away from the classical Gaussian distribution. With 40% noise, the final experimental distribution has made the transition to a Gaussian profile, but the evolution still does not quite match that of the classical evolution. For the highest levels of noise shown (60-200%), the evolutions of the experimental and classical distributions are nearly identical, providing strong evidence that the experiment is behaving classically.

4.6.2.2 Detailed Study: Regime of Classical Anomalous Diffusion

We now focus on a different regime than in the last section. Here we consider the behavior at a peak in the experimental diffusion curve, indicated by the leftmost arrow in Fig. 4.14. This location in the diffusion curve corresponds to a regime of classical anomalous diffusion. As in the previous case, there is a significant difference in the energy after 50 kicks in the absence of noise, as seen in Fig. 4.18. The difference in this figure is much larger than in Fig. 4.14 because of the much later time used in the plot (50 vs. 35 kicks). As noise is applied, the experimental energy increases. This behavior is consistent with the breaking of localization, although it is not completely clear that localization occurs in this regime, because of the nonexponential form of the long-time momentum distributions. By contrast, the classical energy is initially reduced by the applied noise, due to the destruction of the classical correlations. Again, for high noise levels the behavior in the experiment is well described by the classical model.

From the evolution of the energies in Fig. 4.19, we see that the differences between the behaviors of the atoms and the classical model are more subtle than in the case of the previous

section. When there is no applied noise, the experimental data show a faster initial diffusion than one would expect classically; at later times, the diffusion seems to saturate, suggesting that localization effects are setting in, and the diffusion proceeds more slowly than in the classical model. The energy difference in this case is smaller than one might expect from Fig. 4.18, due to slight differences in the intensity and beam diameter of the kicking laser light between the two data runs (notice that this value of K corresponds to a steeply sloped region in the classical diffusion curve). As noise is added, the saturation is less pronounced, until the 40% noise level, where the diffusion occurs more quickly than in the classical model, with little indication of saturation. Above this level, the experiment agrees well with the classical model, and the short-time correlations are evidently small.

The momentum distributions for this case are shown in Fig. 4.20. In the zero-noise case, the experimental distribution after 70 kicks (highlighted in bold) has a characteristic profile,

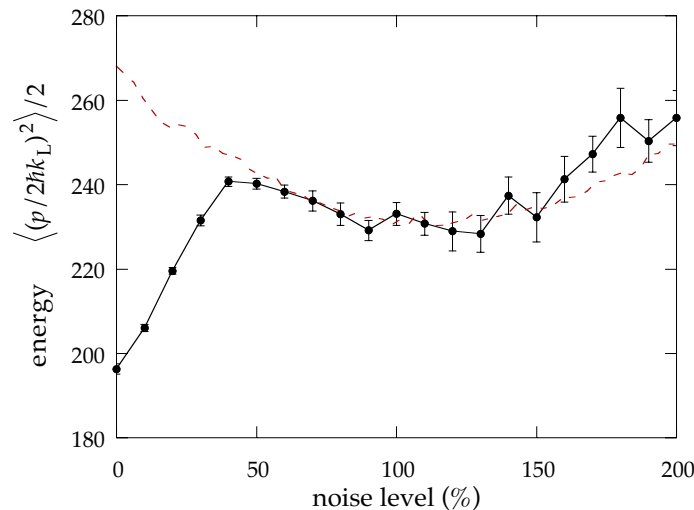


Figure 4.18: Experimentally measured energy (points and solid lines) and energy from the classical model (dashed line) as the noise level is changed, for a fixed time (50 kicks) and stochasticity parameter (the experimental value is $K = 8.4 \pm 10\%$, the classical simulation corresponds to $K = 8.4$). As in the case of Fig. 4.15, there is a large discrepancy between the experimental and classical energies at the lowest noise levels, which disappears for high noise levels. Experimental data are averaged over 18 realizations of noise. The value of K used here corresponds to the leftmost arrow in Fig. 4.14. Note the larger discrepancy for zero noise in this figure, since the time displayed here is later than that used in Fig. 4.14. Note also that the vertical scale used here is magnified compared to that of Fig. 4.15.

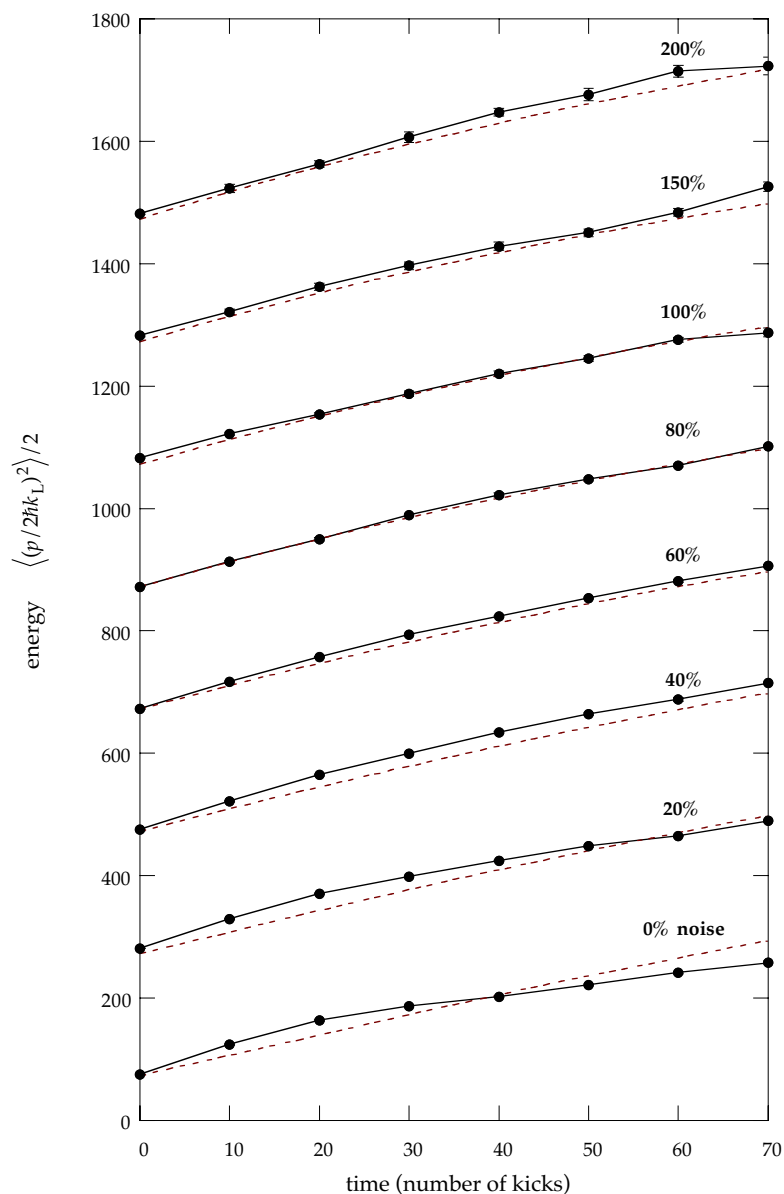


Figure 4.19: Experimentally measured energy (points and solid lines) and energy from the classical model (dashed line) as a function of time, for various levels of applied noise. The experimentally measured stochasticity parameter is $K = 8.4 \pm 10\%$, and the simulation corresponds to $K = 8.7$. The experimental data points are averages over 15 distinct realizations of amplitude noise, and data for successive noise levels are offset vertically by 200 for clarity. The agreement between the experimental data and the classical model is again excellent for noise levels of 60% and above. The value of K used here corresponds to the leftmost arrow in Fig. 4.14.

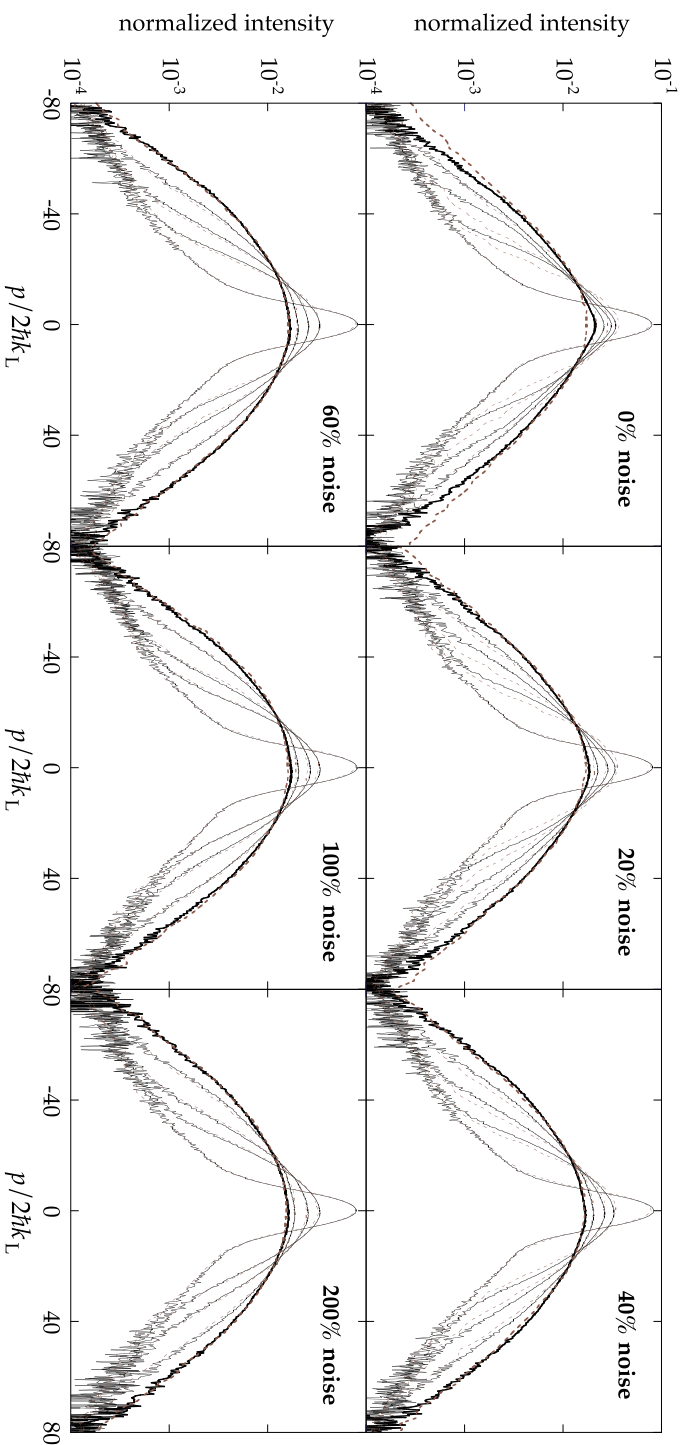


Figure 4.20: Evolution of the momentum distributions, for both the experiment (solid) and classical model (dashed), at various levels of applied noise. The experimentally measured stochasticity parameter is $K = 8.4 \pm 10\%$, and the simulation corresponds to $K = 8.7$. The times shown, in order of increasing width, are 0, 10, 20, 40, and 70 kicks, with the final distributions emphasized in bold. In the zero-noise case, the quantum distribution does not exhibit exponential localization, as observed in previous work, but the behavior is distinctly nonclassical. For the largest three levels of noise shown, the experimental and classical distributions are again nearly indistinguishable. The data and simulations presented in this figure are the same as those used to calculate the energies in Fig. 4.19, and the value of K used here corresponds to the leftmost arrow in Fig. 4.14 (the “peak” in the experimental curve).

rounded and nonexponential in shape. One might be tempted to attribute this shape to the systematic effects that we have discussed, which affect the tails of an exponential distribution with a very long localization length. However, the region over which the distribution is rounded is well within the domain where the systematic effects are not significant. The final classical distribution also has tails that extend well beyond those of the experimental measurement. As noise is introduced, the experimental profile becomes more Gaussian, and the classical diffusion rate is reduced slightly. As in the previous section, the final experimental distribution for 40% noise is Gaussian, but the evolution does not quite proceed at the same rate (as one can most readily see from the distributions at intermediate times). The difference, though, is that the quantum diffusion occurs more quickly than the classical expectation, whereas in the previous section the diffusion occurred more slowly than in the classical model. Again, for the highest levels of noise shown (60-200%), the experimental evolutions are in excellent agreement with the classical model, and hence classical behavior is restored.

4.7 Comparison with a Universal Theory of Quantum Transport

Beyond examining the problem of quantum–classical correspondence, these experimental results are also useful for studying details of quantum transport. Specifically, we can compare these results with a recent quantum diffusion theory by Jianxin Zhong, Roberto Diener, Qian Niu, and others [Zhong01]. This theory concerns the shape of the tails of a spreading quantum wave packet, described by the stretched exponential function

$$P(x, t) \sim \exp(-|x/w|^\gamma) , \quad (4.61)$$

where $w(t)$ is the time-dependent width parameter. The exponent γ here is stationary, and is within the range $[1, \infty)$. This diffusion theory then relates this exponent to the scaling exponent for the width parameter,

$$w(t) \sim t^\beta , \quad (4.62)$$

via the universal relation

$$\gamma = 1/(1 - \beta) . \quad (4.63)$$

This relation is expected to hold for lattice-type models with Schrödinger equations of the form

$$i\partial_t\psi(n,t) = V(n)\psi(n,t) + \sum_{n'} h(n,n')\psi(n',t) , \quad (4.64)$$

where $\psi(n,t)$ is the amplitude at the n th lattice site, $V(n)$ is the lattice-site potential energy, and $h(n,n')$ is the “hopping integral,” which describes the couplings between the sites (for the common “tight-binding” models, only nearest-neighbor sites are directly coupled). As we mentioned above, the kicked rotor can be written in this form, where the lattice describes the ladder in momentum space, and so this spatial-diffusion picture describes the momentum transport in the kicked rotor. This theory has been justified on the basis of numerical simulations in a variety of systems, as well as a general theoretical argument based on a stationary-phase approximation in the coarse-grained generalized master equation [Zhong01], and is valid asymptotically in the tails of the distributions at long times.

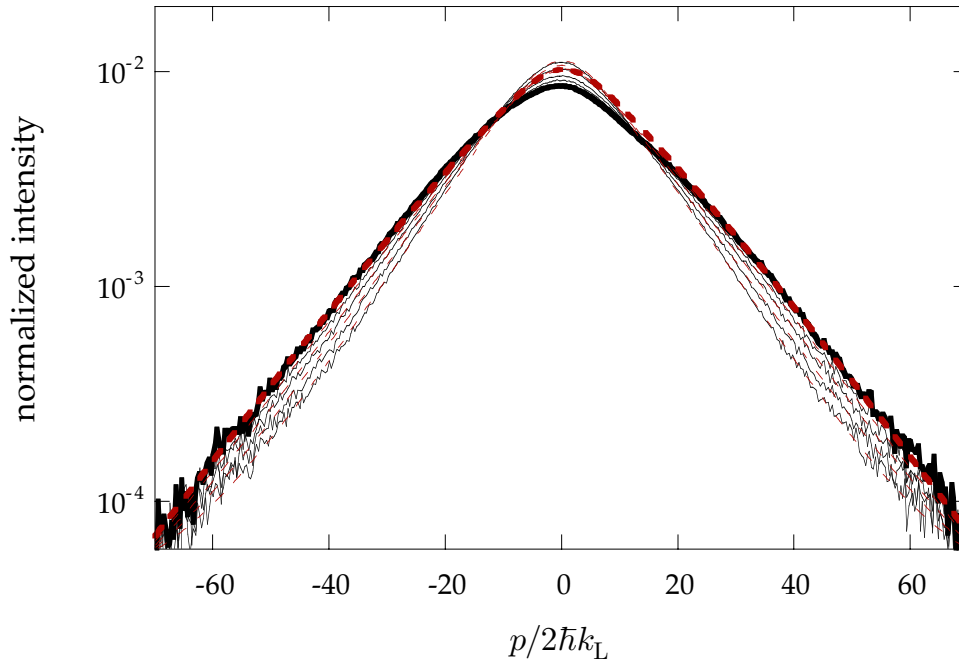


Figure 4.21: Comparison of the diffusion theory in Eqs. (4.61-4.63) to the experimental momentum distribution evolution, for the exponentially localized case. The experimental distributions for $K = 11.2$, $\hbar = 2.08$, and times of 30, 40, 50, 60, and 70 kicks are shown as solid lines, and the simultaneous best fit to the tails of all the distributions is shown as dashed lines. The 70 kick cases are highlighted in bold. The fitted exponents here are $\gamma = 1.06 \pm 0.19$ and $\beta = 0.06 \pm 0.17$, in good agreement with the expectations for dynamical localization.

This theory makes sense in several situations that we have already discussed, such as exponential localization ($\gamma = 1, \beta = 0$), noise-induced (classical-like) diffusion ($\gamma = 2, \beta = 1/2$), and ballistic transport ($\gamma \rightarrow \infty, \beta \rightarrow 1$). What is more interesting, though, is that the universal relation should also hold in the intermediate cases of “quantum anomalous diffusion.” Since we have observed a case of quantum transport (the behavior at the peaks of the diffusion curves, as in Fig. 4.11) that does not fall cleanly in any of the extreme cases, it is interesting to use this theory to study this case.

To compare the theory with the experimental results, we have performed fits of the distributions (4.61) to experimental distributions at 30, 40, 50, 60, and 70 kicks. To focus on the asymptotic behavior, we excluded the data at the earlier times (0, 10, and 20 kicks), and the center portions of the data (bounded by $|p/2\hbar k_L| \sim 15$) were also excluded. The distributions

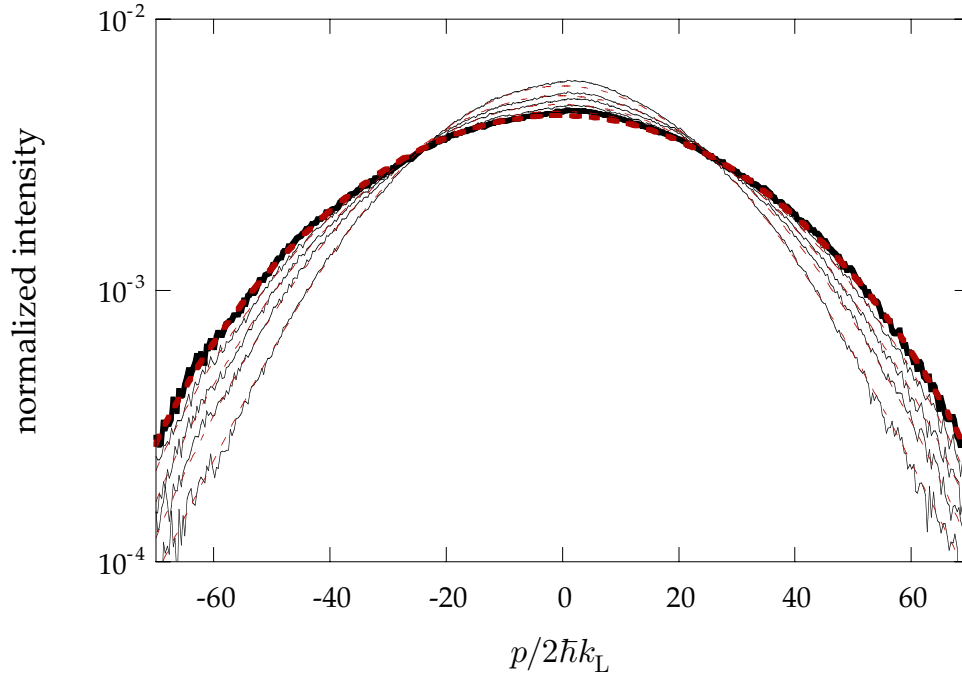


Figure 4.22: Comparison of the diffusion theory in Eqs. (4.61-4.63) to the experimental momentum distribution evolution, for a case driven by 200% amplitude noise. The experimental distributions for $K = 11.2$, $k = 2.08$, and times of 30, 40, 50, 60, and 70 kicks are shown as solid lines, and the simultaneous best fit to the tails of all the distributions is shown as dashed lines. The 70 kick cases are highlighted in bold. The fitted exponents here are $\gamma = 2.03 \pm 0.14$ and $\beta = 0.51 \pm 0.03$, consistent with normal (classical) diffusion.

were likewise truncated outside $|p/2\hbar k_L| \sim 70$ to exclude the regions of poor signal-to-noise ratio that might have skewed the fits. All the distributions for a given case were fit simultaneously, using a common fitting exponent γ . The scaling relation (4.62) was enforced by the constraint

$$w(t) = w_0 + \alpha t^\beta, \quad (4.65)$$

where w_0 and α are fitting parameters, and β was constrained by the relation (4.63). In the fit, each distribution was convolved with the initial momentum distribution and then corrected for the known response of the detection system (i.e., the nonuniformity of the Gaussian imaging laser beams). To account for shot-to-shot variations in the backgrounds of the CCD camera photographs, it was necessary to include the vertical offsets and the amplitudes of the distributions as fitting parameters. The fits were stabilized by constraining vertical offsets to a two-parameter linear model and the amplitudes to a three-parameter quadratic model; these constraints were

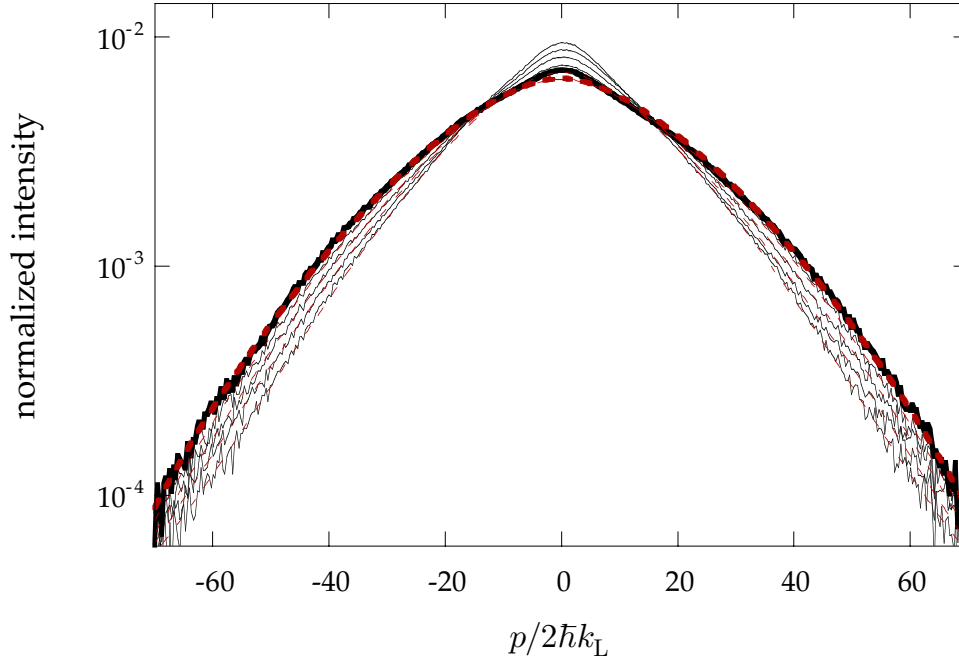


Figure 4.23: Comparison of the diffusion theory in Eqs. (4.61-4.63) to the experimental momentum distribution evolution, for the case influenced by classical anomalous transport. The experimental distributions for $K = 8.4$, $\hbar k = 2.08$, and times of 30, 40, 50, 60, and 70 kicks are shown as solid lines, and the simultaneous best fit to the tails of all the distributions is shown as dashed lines. The 70 kick cases are highlighted in bold. The fitted exponents here are $\gamma = 1.48 \pm 0.16$ and $\beta = 0.32 \pm 0.07$, consistent with quantum anomalous diffusion.

justified on physical grounds and on the basis of fits where these parameters were treated independently. The other effects discussed in Section 4.6.1 were not explicitly accounted for, and thus influenced the values of the fitted parameters. In order to emphasize the tails of the distribution during the fit, the logarithms of the data were computed before being sent to the Marquardt-Levenberg fitting routine. The uncertainties quoted here primarily reflect the sensitivity of the fits to the choice of cutoff locations.

We have applied this fit to three sets of data. The first corresponds to exponential localization (Fig. 4.21), where the fitted exponents were $\gamma = 1.06 \pm 0.19$ and $\beta = 0.06 \pm 0.17$. These values are consistent with the expected values. The second case is the strongest case (200%) of amplitude noise that we considered above (Fig. 4.22), where the fitted values of $\gamma = 2.03 \pm 0.14$ and $\beta = 0.51 \pm 0.03$ are also consistent with the expected values for regular diffusion. Finally, in the regime of classical anomalous diffusion (Fig. 4.23), the fitted values were $\gamma = 1.48 \pm 0.16$ and $\beta = 0.32 \pm 0.07$, indicating intermediate behavior of quantum anomalous diffusion. In all three cases, the tails of the experimental distributions match very well with the fitted distributions.

4.8 Calculation of the Correlations

We will now run through the calculation of the correlations that we have used in this chapter. These correlations were calculated using probabilistic methods [Rechester80], including an elegant path-summation method [Rechester81], but here we will follow the direct approach used by Shepelyansky [Shepelyanskii82] for calculating the quantum correlations.

4.8.1 Classical Correlations

Beginning with the generalized standard map,

$$\begin{aligned} p_{n+1} &= p_n + K_n \sin x_n \\ q_{n+1} &= q_n + p_{n+1} \end{aligned} \quad (4.66)$$

which allows for different kick strengths on each iteration, we wish to calculate the correlation function

$$C_n := \langle K_0 \sin x_0 K_n \sin x_n \rangle, \quad (4.67)$$

where we will take the average over the initial distribution to be uniform over phase space. To evaluate this function, we need to calculate the exponentials e^{ix_m} of the iterated coordinates, in view of the form

$$C_n = K_0 K_n \langle e^{ix_0} e^{ix_n} - e^{ix_0} e^{-ix_n} \rangle + \text{c.c.} \quad (4.68)$$

of the correlation functions.

We will proceed by calculating the first few correlations before generalizing to the arbitrary case. If we use the generating function for the Bessel functions $J_n(x)$,

$$\exp \left[\left(t - \frac{1}{t} \right) \frac{z}{2} \right] = \sum_s J_s(z) t^n, \quad (4.69)$$

we can let $t = \exp(ix)$ and $z = K$ to obtain

$$\exp(iK \sin x) = \sum_s J_s(K) e^{isx}. \quad (4.70)$$

This relation allows the evaluation of the first iterated exponential,

$$\begin{aligned} e^{ix_1} &= \exp[i(x_0 + p_0 + K_0 \sin x_0)] \\ &= \sum_{s_0} J_{s_0}(K_0) e^{i(s_0+1)x_0} e^{ip_0}. \end{aligned} \quad (4.71)$$

We can iterate this procedure to obtain the next two exponentials. After reversing the order of the indices, we obtain

$$\begin{aligned} e^{ix_2} &= \sum_{s_0, s_1} J_{s_0}[K_1] J_{s_1}[K_0(s_0 + 2)] e^{i(s_1+s_0+1)x_0} e^{i(s_0+2)p_0} \\ e^{ix_3} &= \sum_{s_0, s_1, s_2} J_{s_0}[K_2] J_{s_1}[K_1(s_0 + 2)] J_{s_2}[K_0(2s_0 + s_1 + 3)] \\ &\quad \times e^{i(s_2+s_1+s_0+1)x_0} e^{i(2s_0+s_1+3)p_0} \end{aligned} \quad (4.72)$$

At this stage the pattern of the iteration is apparent. We can define the recurrence relations

$$\begin{aligned} \alpha_0 &= s_0 + 1 \\ \alpha_{n+1} &= \alpha_n + s_{n+1} \end{aligned} \quad (4.73)$$

and

$$\begin{aligned} \beta_0 &= 1 + \alpha_0 \\ \beta_{n+1} &= \beta_n + \alpha_n, \end{aligned} \quad (4.74)$$

and then write the n th iterated exponential as

$$e^{ix_n} = \sum_{s_0 \cdots s_{n-1}} J_{s_0}(K_{n-1}\beta_0) J_{s_1}(K_{n-2}\beta_1) \cdots J_{s_{n-1}}(K_0\beta_{n-1}) e^{i\alpha_{n-1}x_0} e^{i\beta_{n-1}p_0} . \quad (4.75)$$

Now it is straightforward to evaluate the correlations (4.67), as the phase-space averages amount to projections into a Fourier basis, with the general result

$$C_n = \frac{K_0 K_n}{2} \sum_{s_0 \cdots s_{n-1}} J_{s_0}(K_{n-1}\beta_0) J_{s_1}(K_{n-2}\beta_1) \cdots J_{s_{n-1}}(K_0\beta_{n-1}) \times (\delta_{\alpha_{n-1},1} - \delta_{\alpha_{n-1},-1}) \delta_{\beta_{n-1},0} , \quad (4.76)$$

where $\delta_{n,n'}$ is the Kronecker symbol. Thus, the first few correlations evaluate to

$$\begin{aligned} C_0 &= \frac{K_0^2}{2} \\ C_1 &= 0 \\ C_2 &= -\frac{K_0 K_2}{2} J_2(K_1) \\ C_3 &= \frac{K_0 K_3}{2} [J_3(K_1) J_3(K_2) - J_1(K_1) J_1(K_2)] \\ C_4 &= \frac{K_0 K_4}{2} [J_2(K_1) J_2(K_3) + O(K^{-3/2})] , \end{aligned} \quad (4.77)$$

where K is the statistical average of the K_n . For the normal standard map, $K_n = K$ for all n , and inserting these correlations into Eq. (4.20), we recover the diffusion rate (4.24). On the other hand, for amplitude noise, it is appropriate to average the K_n over their probability distributions, as in (4.28). Doing so, we recover the noise-modified diffusion result (4.29). Notice that for the case of uniformly distributed amplitude noise, Eq. (4.29) can be integrated analytically, with the somewhat unenlightening result,

$$\begin{aligned} D(K, \delta K_{p-p}) &= \frac{K^2}{4} + \frac{\delta K_{p-p}^2}{48} \\ &+ \frac{K^2}{2} \left\{ -\mathcal{J}_2(K, \delta K_{p-p}) + \mathcal{J}_2^2(K, \delta K_{p-p}) \right. \\ &+ \frac{4}{\delta K_{p-p}} [J_2(K^+) - J_2(K^-)]^2 \\ &\left. - \frac{4}{\delta K_{p-p}} [J_0(K^+) - J_0(K^-)] [J_2(K^+) - J_2(K^-)] \right\} , \end{aligned} \quad (4.78)$$

where $K^\pm := K \pm \delta K_{p-p}/2$,

$$\begin{aligned} \mathcal{J}_2(K, \delta K_{p-p}) = \frac{1}{\delta K_{p-p}} & \left\{ K^+ J_0(K^+) - K^- J_0(K^-) - 2[J_1(K^+) - J_1(K^-)] \right. \\ & - \frac{\pi}{2} [J_0(K^+) \mathbf{H}_1(K^+) - J_1(K^+) \mathbf{H}_0(K^+)] \\ & \left. + \frac{\pi}{2} [J_0(K^-) \mathbf{H}_1(K^-) - J_1(K^-) \mathbf{H}_0(K^-)] \right\} , \end{aligned} \quad (4.79)$$

and the $\mathbf{H}_n(x)$ are the Struve functions of order n .

4.8.2 Quantum Correlations

The calculation of the quantum correlations follows along similar lines to the classical calculation, but is somewhat more complex. The derivation here follows the work of Shepelyansky [Shepelyanskii82; Shepelyansky87]. The goal here is to calculate the (symmetrized) quantum correlation function

$$C_{q,n} = \frac{K_0 K_n}{2} \langle \psi_0 | (\sin x_n \sin x_0 + \sin x_0 \sin x_n) | \psi_0 \rangle , \quad (4.80)$$

which is averaged with respect to the initial state $|\psi_0\rangle$. The coordinates x_n and p_n here are Heisenberg-picture operators, which obey equations formally equivalent to the classical standard map, as we have indicated above. The initial state is again approximately uniform over phase space, so that

$$\langle \psi_0 | e^{imx_0} e^{inp_0} | \psi_0 \rangle = \delta_{m,0} \delta_{n,0} . \quad (4.81)$$

We begin as before, calculating the first iterated exponential

$$e^{ix_1} = e^{i(x_0 + p_0 + K_0 \sin x_0)} = \exp \left[-p_0 + ix_0 + \frac{K_0}{2} e^{ix_0} - \frac{K_0}{2} e^{-ix_0} \right] . \quad (4.82)$$

To factor this exponential, we use two special cases of the Baker–Campbell–Hausdorff relation [Wilcox67]. The first is

$$\exp(A + B) = \exp \left(B \frac{e^c - 1}{c} \right) \exp(A) \quad (4.83)$$

for operators A and B such that $[A, B] = cB$. The second case is

$$\exp(A + B) = \exp(A) \exp(B) \exp \left(-\frac{1}{2} [A, B] \right) = \exp(B) \exp(A) \exp \left(\frac{1}{2} [A, B] \right) , \quad (4.84)$$

if $[A, [A, B]] = [B, [A, B]] = 0$. After factorization, the result is

$$e^{ix_1} = \exp\left(i\frac{2K_0}{k}\sin(k/2)\sin(x_0 + k/2)\right) e^{ix_0} e^{ip_0} e^{ik/2} . \quad (4.85)$$

We can then apply the identity (4.70), with the result

$$e^{ix_1} = \sum_{s_0} J_{s_0}(K_{q,0}) \exp\left[i\frac{k}{2}(s_0 + 1)\right] e^{i(s_0+1)x_0} e^{ip_0} , \quad (4.86)$$

where $K_{q,0} := K_0 \sin(k/2)/(k/2)$. The general case is then obtained by iterating this relation and then normally ordering the operators (i.e., so that all the p_0 are on the right). Shepelyansky's result is

$$e^{ix_n} = \sum_{s_0 \cdots s_{n-1}} J_{s_0}(K_{q,n-1}\beta_0) J_{s_1}(K_{q,n-2}\beta_1) \cdots J_{s_{n-1}}(K_{q,0}\beta_{n-1}) e^{i\gamma_n} e^{i\alpha_{n-1}x_0} e^{i\beta_{n-1}p_0} , \quad (4.87)$$

where the functions α_n and β_n are defined as before, and we have defined an additional function by the relations

$$\begin{aligned} \gamma_0 &= \frac{k}{2}(s_0 + 1) \\ \gamma_{n+1} &= \gamma_n + \frac{k}{2}s_n(\alpha_n + \beta_n) + \frac{k}{2}\alpha_n^2 . \end{aligned} \quad (4.88)$$

We can then define the function

$$\begin{aligned} R(n, r) &:= \frac{1}{2} \langle \psi_0 | [\exp(-irx_0) \exp(ix_n) + \exp(ix_n) \exp(-irx_0)] | \psi_0 \rangle \\ &= \frac{1}{2} \sum_{s_0 \cdots s_{n-1}} J_{s_0}(K_{q,n-1}\beta_0) J_{s_1}(K_{q,n-2}\beta_1) \cdots J_{s_{n-1}}(K_{q,0}\beta_{n-1}) \\ &\quad \times (1 + e^{-i\beta_{n-1}kq}) e^{i\gamma_n} \delta_{\alpha_{n-1},q} \delta_{\beta_{n-1},0} , \end{aligned} \quad (4.89)$$

in terms of which we can write the correlation function as

$$C_{q,n} = \frac{K_0 K_n}{4} [R(n, -1) - R(n, 1)] + \text{c.c.} . \quad (4.90)$$

The first few of these quantum correlations evaluate to

$$\begin{aligned}
C_{q,0} &= \frac{K_0^2}{2} \\
C_{q,1} &= 0 \\
C_{q,2} &= -\frac{K_0 K_2}{2} J_2(K_{q,1}) \\
C_{q,3} &= \frac{K_0 K_3}{2} [J_3(K_{q,1}) J_3(K_{q,2}) - J_1(K_{q,1}) J_1(K_{q,2})] \\
C_{q,4} &= \frac{K_0 K_4}{2} [J_2(K_{q,1}) J_2(K_{q,3}) + O(K_q^{-3/2})] ,
\end{aligned} \tag{4.91}$$

Hence, we see that the first few quantum correlations have essentially the same form as the classical correlations in Eqs. (4.77), but with the quantum scaling factor applied to the arguments of the Bessel functions. The diffusion-rate results in the case of the normal quantum kicked rotor (4.47) and the amplitude-noise case (4.49) then proceed as in the classical case.